https://doi.org/10.1038/s41586-019-1175-6

Aqueous Li–ion battery enabled by halogen conversion–intercalation chemistry in graphite

Chongyin Yang[1,7], Ji Chen[1,7], Xiao Ji[1], Travis P. Pollard[2], Xujie Lü[3], Cheng-Jun Sun[4], Singyuk Hou[1], Qi Liu[4,5], Cunming Liu[4], Tingting Qing[1], Yingqi Wang[3], Oleg Borodin[2], Yang Ren[4], Kang Xu[2] & Chunsheng Wang[1,6]*

The use of 'water-in-salt' electrolytes has considerably expanded the electrochemical window of aqueous lithium-ion batteries to 3 to 4 volts, making it possible to couple high-voltage cathodes with low-potential graphite anodes[1–4]. However, the limited lithium intercalation capacities (less than 200 milliampere-hours per gram) of typical transition-metal-oxide cathodes[5,6] preclude higher energy densities. Partial[7,8] or exclusive[9] anionic redox reactions may achieve higher capacity, but at the expense of reversibility. Here we report a halogen conversion–intercalation chemistry in graphite that produces composite electrodes with a capacity of 243 milliampere-hours per gram (for the total weight of the electrode) at an average potential of 4.2 volts versus Li/Li$^+$. Experimental characterization and modelling attribute this high specific capacity to a densely packed stage-I graphite intercalation compound, $C_{3.5}[Br_{0.5}Cl_{0.5}]$, which can form reversibly in water-in-bisalt electrolyte. By coupling this cathode with a passivated graphite anode, we create a 4-volt-class aqueous Li-ion full cell with an energy density of 460 watt-hours per kilogram of total composite electrode and about 100 per cent Coulombic efficiency. This anion conversion–intercalation mechanism combines the high energy densities of the conversion reactions, the excellent reversibility of the intercalation mechanism and the improved safety of aqueous batteries.

Using the anionic-redox reaction of halide anions (Br^- and Cl^-) in graphite, a composite electrode containing equimolar lithium halide salts $(LiBr)_{0.5}(LiCl)_{0.5}$–graphite (hereafter denoted as LBC-G) was synthesized by mixing anhydrous LiBr and LiCl with graphite at an optimal mass ratio of 2:1:2 (corresponding to a molar ratio of $(LiBr)_{0.5}(LiCl)_{0.5}C_{\sim 3.7}$; see Methods). Herein, the highly concentrated water-in-bisalt (WIBS) electrolyte confined partially hydrated LiBr/LiCl within the solid cathode matrix, and upon oxidation, Br^0 and Cl^0 are stabilized by sequential intercalation into the graphite host as solid graphite intercalation compounds (GICs). This new cathode chemistry inherits the high energy of the conversion reaction and the excellent reversibility of topotactic intercalation, and provides batteries that differ fundamentally from the 'dual-ion' batteries that reversibly intercalate complex anions (PF_6^-, BF_4^-, $TFSI^-$; TFSI, bis(trifluoromethanesulfonyl)imide) into graphite at low packing density, where these stable anions experience no redox reactions, resulting in low capacities[10,11] below 120 mAh g^{-1}.

Upon exposure to water-in-bisalt (WiBS) electrolyte, the anhydrous LiBr/LiCl extracts approximately 2.4% water from WiBS (Extended Data Fig. 1a, b) forming a hydrated LiBr/LiCl layer on the LBC-G surface (illustrated in Fig. 1a; estimated overall formulations of hydrated salts: $LiBr{\cdot}0.34H_2O$-$LiCl{\cdot}0.34H_2O$; electrode:electrolyte = 1:20), which accelerates the halogens' redox reaction in the form of liquefied anions. Owing to the immiscibility of halide anions in WiBS, this hydrated layer is thermodynamically phase-separated from the bulk electrolyte and builds dynamic water equilibrium (Extended Data Fig. 1c), as previously observed for lithium polysulfides[4]. Such a liquefied layer allows fast Li^+ transport but confines all the halide anions within the cathode, as evidenced by both molecular dynamics (MD) simulations (Extended Data Fig. 1d) and the extremely low Cl/Br content (<32 p.p.m.) detected by chromatographic analysis in WiBS equilibrated with LiCl/LiBr solution for 500 h (Extended Data Fig. 1e).

The electrochemical behaviours of LBC-G were first evaluated in a three-electrode cell with an aqueous gel polymer electrolyte based on WiBS (see Methods). The cyclic voltammetry (Fig. 1b) and charge/discharge profiles (Fig. 1c, d) indicated two distinct reaction voltage ranges, 4.0–4.2 V for Br^- intercalation and 4.2–4.5 V for Cl^- intercalation, which deliver a highly reversible discharge capacity of 243 mAh g^{-1} (for the total mass of LBC-G composite), 82% of which is retained over 230 cycles at a Coulombic efficiency of 100% after the 80th cycle at a current density of 80 mA g^{-1} (0.2 C). The two-step redox reactions correspond to (Fig. 1a):

$$LiBr + C_n \leftrightarrow C_n[Br] + Li^+ + e^- \quad 4.0\text{–}4.2\,V \tag{1}$$

$$LiCl + C_n[Br] \leftrightarrow C_n[BrCl] + Li^+ + e^- \quad 4.2\text{–}4.5\,V \tag{2}$$

where n is the molar ratio of carbon atoms to the intercalated halogens in the GIC. Upon charging, Br^- is the first species within the hydration layer to oxidize to a near-zero state (Br^0) and to intercalate into graphite, forming $C_n[Br]$ (equation (1)). Further charging oxidizes and intercalates Cl^- (equation (2)), forming a mixed intercalation compound, $C_n[BrCl]$. The oxidation of each halogen involves a one-electron transfer reaction (theoretical capacity: 309 mAh g^{-1} for LiBr, 632 mAh g^{-1} for LiCl)[12] and the release of one Li^+ into the bulk electrolyte. Upon discharging, the reverse process occurs: Cl^0 and Br^0 successively de-intercalate from the graphite interlayer, reduce into halides and recombine with Li^+ to form both solid LiCl/LiBr crystals and liquefied halides outside of the graphite interlayer (Extended Data Fig. 2a–d). WiBS plays another essential role in this chemistry by pushing the oxidation potential of water to about 4.9 V versus Li/Li$^+$ (refs [1,3]), realizing full reversibility of the halide oxidation/reduction without electrolyte decomposition (Extended Data Fig. 3).

The galvanostatic intermittent titration technique (GITT) was used to examine the quasi-equilibrium potentials and kinetics of reactions at different stages. The quasi-equilibrium potentials are about 4.05 V for Br^- and about 4.35 V for Cl^- oxidation/intercalation, respectively (Fig. 1e), whereas the total diffusion coefficients were estimated to be 10^{-15}–10^{-13} cm^2 s^{-1} (red and blue curves in the inset of Fig. 1e). The diffusion coefficients were also estimated with electrochemical impedance spectroscopy (EIS; Fig. 1f), and fitting with the equivalent circuit in Extended Data Fig. 4a yielded apparent ionic diffusion coefficients of 6.85×10^{-15}–2.07×10^{-14} cm^2 s^{-1} (green circles in the inset of Fig. 1e), in excellent agreement with the GITT results. Considering the extremely high diffusion coefficients of halogens in the graphite interlayer[13] (EIS independence of graphite size shown in Extended Data Fig. 4b),

[1]Department of Chemical and Biomolecular Engineering, University of Maryland, College Park, MD, USA. [2]Electrochemistry Branch, Power and Energy Division, Sensor and Electron Devices Directorate, US Army Research Laboratory, Adelphi, MD, USA. [3]Center for High Pressure Science and Technology Advanced Research, Shanghai, China. [4]X-ray Science Division, Advanced Photon Source, Argonne National Laboratory, Argonne, IL, USA. [5]Department of Physics, City University of Hong Kong, Hong Kong, China. [6]Department of Chemistry and Biochemistry, University of Maryland, College Park, MD, USA. [7]These authors contributed equally: Chongyin Yang, Ji Chen. *e-mail: cswang@umd.edu

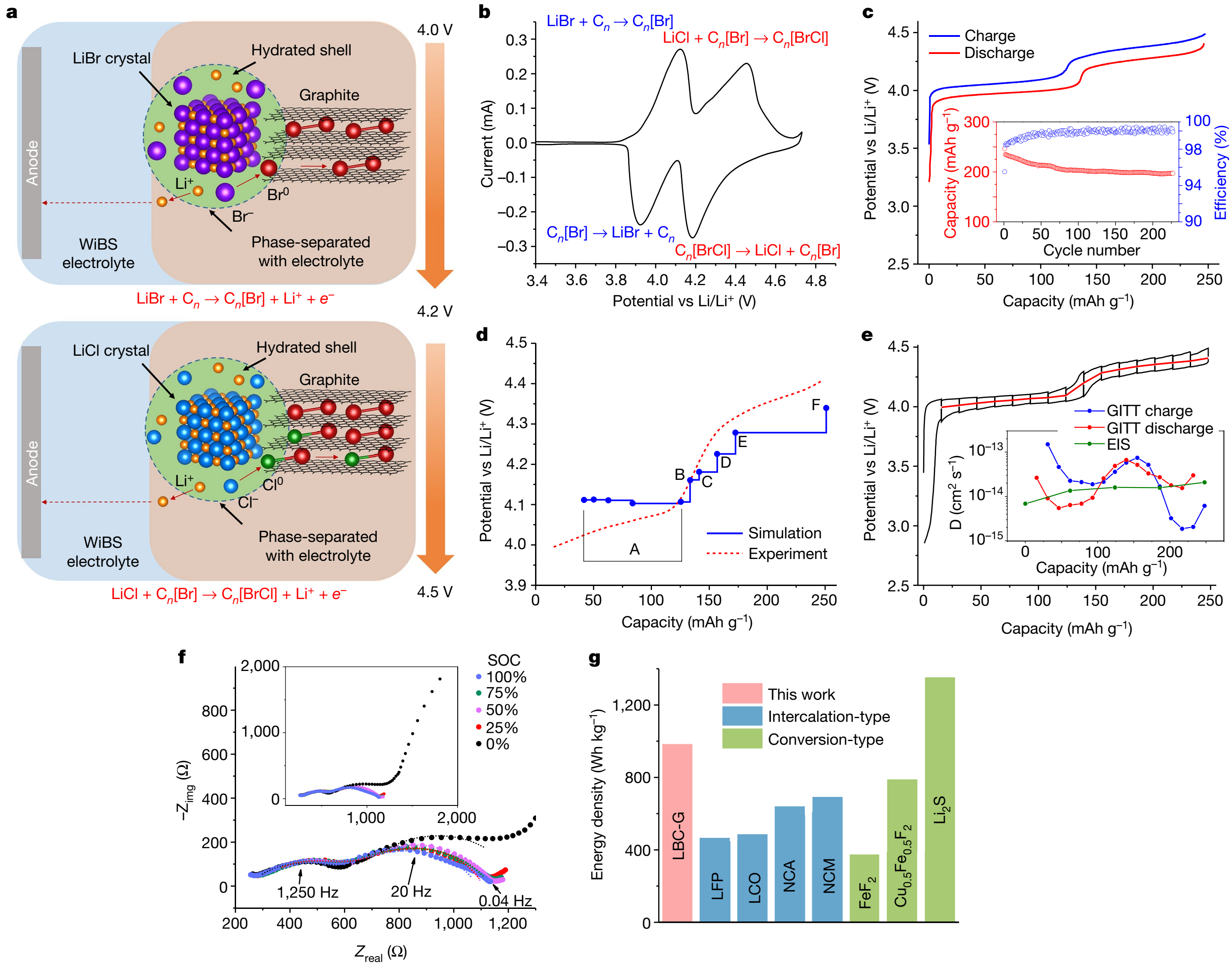

Fig. 1 | Proposed conversion–intercalation chemistry. a, Schematic of the conversion–intercalation mechanism occurring in the LBC-G composite during its oxidation in WiBS aqueous-gel electrolyte. The two-stage reactions involve the oxidation of Br^- (about 4.0 V) and Cl^- (about 4.2 V) and their subsequent intercalation into the graphitic structure. The discharge is a complete reversal of the charge process. **b**, Cyclic voltammogram of the LBC-G cathode between potentials of 3.2 V and 4.9 V versus Li/Li^+, obtained at a scan rate of 0.05 mV s^{-1}. **c**, Galvanostatic charge/discharge profiles of the LBC-G cathode at a current density of 80 mA g^{-1}. Inset, discharge capacity retention and Coulombic efficiency. **d**, Comparison between the intercalation voltage predicted by density functional theory (DFT) simulations and the quasi-equilibrium voltage curves obtained from GITT measurements (Fig. 1e). The data points of the simulations are: stage-VI C_{20}[Br], stage-V $C_{17.5}$[Br], stage-IV C_{14}[Br], stage-III $C_{10.5}$[Br] and stage-II C_7[Br] (A); stage-I $C_{3.5}[Br_{0.9375}Cl_{0.0625}]$ (B); stage-I $C_{3.5}[Br_{0.875}Cl_{0.125}]$ (C); stage-I $C_{3.5}[Br_{0.75}Cl_{0.25}]$ (D); stage-I $C_{3.5}[Br_{0.625}Cl_{0.375}]$ (E); and stage-I $C_{3.5}[Br_{0.5}Cl_{0.5}]$ (F). **e**, GITT characterization of the LBC-G cathode at a current density of 80 mA g^{-1}. The red curve indicates the quasi-equilibrium potential at different lithiation/de-lithiation stages, which was constructed from the average value of each open-circuit voltage period during charge/discharge. Inset, the finite diffusion coefficients D of the reactants, estimated from GITT and EIS measurements (see Methods). **f**, Nyquist plots for the LBC-G cathode, obtained by EIS tests at various SOCs in a three-electrode cell. The dotted lines are fitting curves obtained by using the equivalent circuit shown in Extended Data Fig. 4a. Inset, the same plots in full scale. Z_{real} and Z_{img} are the real and imaginary parts of the impedance, respectively. **g**, Practical gravimetric energy density of the LBC-G cathode compared with that of representative state-of-the-art cathodes, with average discharge voltages referred to Li/Li^+. Intercalation-type[6]: $LiFePO_4$ (LFP), $LiCoO_2$ (LCO), $LiNi_{0.8}Co_{0.15}Al_{0.05}O_2$ (NCA), $LiNi_{0.8}Co_{0.1}Mn_{0.1}O_2$ (NCM); conversion-type[9,12]: FeF_2, $Cu_{0.5}Fe_{0.5}F$, Li_2S. The values were calculated from the reversible gravimetric capacities using the total mass of the cathode (including active, inactive and polymeric binder) and average discharge voltages. The mass ratios of the active materials are 90% for intercalation-type cathodes, 70% for metal fluorides and 50% for sulfur.

the mass transfer of Br^- and Cl^- between solid salts and the graphite surface constitutes the rate-determining step in this chemistry.

Figure 1g compares gravimetric energy densities of the LBC-G composite with state-of-the-art cathode materials. LBC-G provides a practical gravimetric capacity of 231 mAh g^{-1} (for the total weight of the electrode) and volumetric capacity of 450 mAh mL^{-1} (total volume of the electrode) at an average discharge voltage of 4.2 V, yielding an unprecedented energy density of 970 Wh kg^{-1}, almost twice as high as that of transition-metal intercalation cathodes. Although sulfur conversion chemistry provides comparable gravimetric energy density, LBC-G is much superior per volume because of its more compact storage of halogens in the graphite interlayer (Extended Data Fig. 4c).

In situ Raman spectroscopy (100–550 cm^{-1}) was performed to probe the intercalation mechanism of halogen into graphite (Fig. 2a). With the state of charge (SOC) at 0%–50%, a characteristic peak (at frequency $\omega_0 = 242$ cm^{-1}) was detected, which corresponds[14] to the stretch-mode of intercalated Br_2. Further charging introduced a feature corresponding to the BrCl intercalant ($\omega_0 = 310$ cm^{-1}), verified by a reference prepared by chemical intercalation of BrCl into the graphite (Extended Data Fig. 6g). The peak intensity of the BrCl intercalant

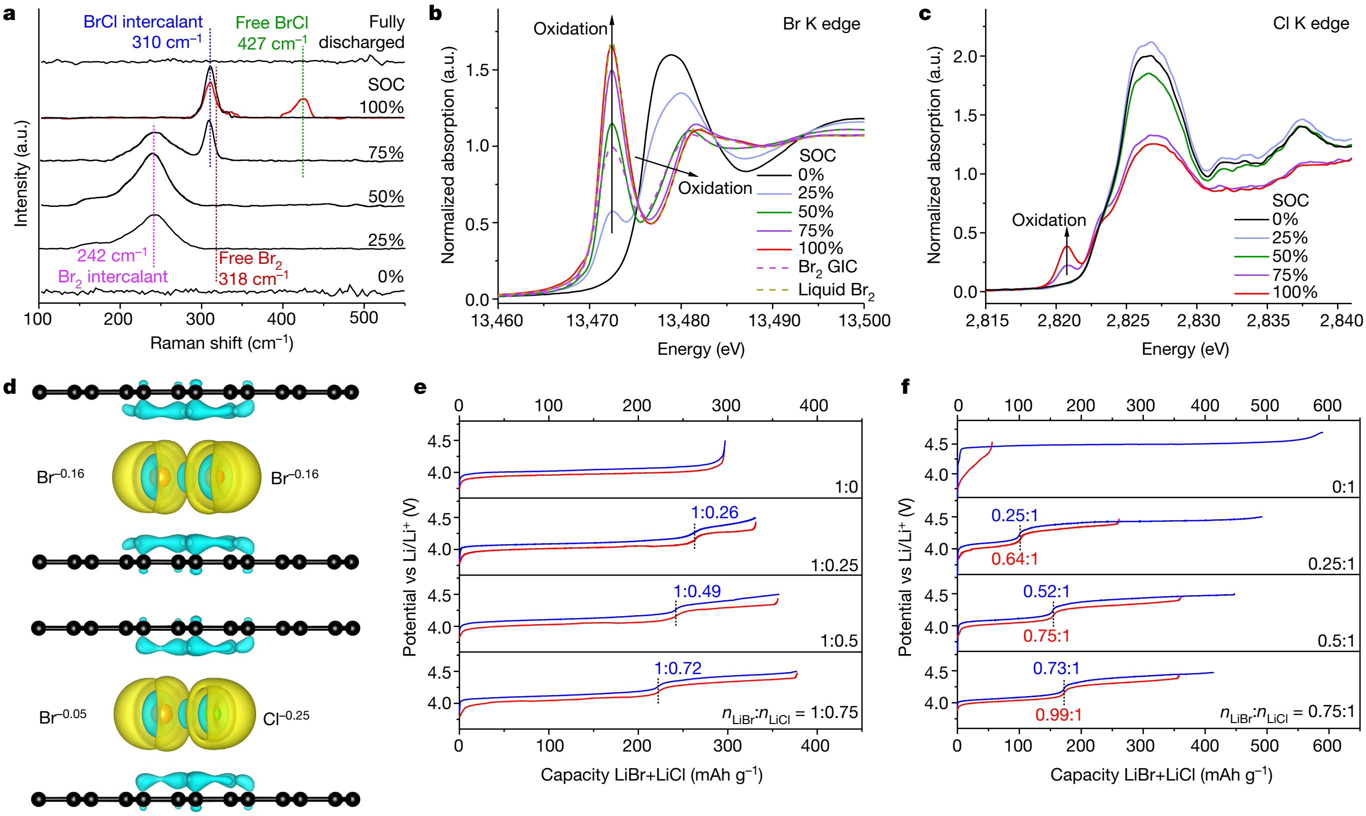

Fig. 2 | Br and Cl conversion–intercalation mechanism. **a**, Raman spectra (100–550 cm^{-1}) of LBC-G obtained in situ during the entire charge–discharge cycle, showing the evolutions of the Br_2 and BrCl intercalants. The red line corresponds to free-BrCl signals, which were detected only after deliberately destabilizing the graphite host with a strong laser beam, further confirming the BrCl intercalation. Background from quartz has been removed. **b**, Br K-edge XANES spectra of LBC-G composite obtained ex situ during the first charging process. Control samples of chemically intercalated Br_2 and liquid Br_2 (dashed curves) were measured in the same cell configuration. **c**, Cl K-edge XANES spectra of LBC-G composite acquired ex situ during the first charging process. **d**, Isosurface of the charge-density difference for GICs $C_n[Br]$ (top) and $C_n[BrCl]$ (bottom) obtained from DFT simulations. Yellow and blue regions represent the accumulation and depletion of electrons compared with Br_2 and BrCl gas molecules (isovalue of $\pm 0.0006e$ Å^{-3}; e, electron charge), respectively. The oxidation states obtained from Bader analysis are: −0.16 for Br in $C_n[Br]$; −0.05 for Br and −0.25 for Cl in $C_n[BrCl]$. **e**, **f**, Charge/discharge profiles of LBC-G composites with various molar ratios of LiBr/LiCl after the first charge at a current density of 80 mA g^{-1}. The specific capacities were estimated according to the weight of LiBr and LiCl. The molar ratios were changed by reducing the fractions of LiCl (**e**) or LiBr (**f**) compared with the original LiBr/LiCl/graphite composites.

increased with charging of LBC-G to 4.5 V. The interaction with the graphene layer weakened the interatomic bonds of halogen intercalants, causing a frequency downshift from 318 cm^{-1} for free Br_2 (liquid) to 242 cm^{-1} for the Br_2 intercalant, and from 427 cm^{-1} for free BrCl (gaseous) to 310 cm^{-1} for the BrCl intercalant[15,16]. We note that during charging/discharging between 3.2 V and 4.5 V, no free Br_2 or BrCl peaks were detected, unless we deliberately destabilized the fully intercalated BrCl-GIC with a high-intensity laser beam (red curve in Fig. 2a); this suggests that all the halogens were intercalated into the graphite structure rather than absorbing on its surface. Upon discharging, the original Raman spectra were restored, demonstrating the reversibility of LCC-G chemistry.

Ex situ X-ray absorption near-edge structure (XANES) spectra reveal how the redox reaction sequence of halogens occurs in the LBC-G cathode (Fig. 2b). For the Br K edge, a distinct and sharp peak at about 13,473 eV, attributed to the Br intra-atomic $1s \rightarrow 4p$ transition, appeared immediately upon charging. The intensity of this peak, which reflects the hole density of Br $4p$ orbitals, gradually increased, accompanied by a blue-shifted absorption edge ($1s \rightarrow$ continuum)[17]. This provides clear evidence that Br^- accepts a hole to be oxidized to Br^0. For the Cl K edge (Fig. 2c), only a single absorption edge ($1s \rightarrow$ continuum) was observed at the first charge plateau (SOC 0%–50%), indicating that all Cl remained[18] as Cl^-. Cl^- oxidation occurred only at the second charge plateau (SOC 50%–100%), as demonstrated by the appearance of the Cl intra-atomic $1s \rightarrow 3p$ transition peak (about 2,821 eV) due to the removal of a hole by Cl^-. By comparing with the reference spectra (dashed lines in Fig. 2b) of chemically intercalated Br_2-GIC and liquid Br_2, we see that Br was mostly oxidized, but had not entirely reached Br^0 at the first charge plateau (SOC 0%–50%). Both density functional theory (DFT) simulations (Fig. 2d) and the literature[19] suggest that Br remains at an oxidation state of approximately −0.16 in Br_2-GICs at 50% SOC. Only after the subsequently intercalated Cl associates with previously intercalated Br does the Br-oxidation state further increase to nearly Br^0 (oxidation state −0.05), owing to the lower electron negativity of Br relative to Cl. The oxidation state of Cl becomes −0.25.

Additional evidence supporting this conversion–intercalation mechanism comes from the charge/discharge profiles of LBC-G at different LiBr/LiCl molar ratios (Fig. 2e, f). The capacity ratios of the two charge/discharge plateaus are highly correlated with the LiBr/LiCl molar ratio. The specific capacities calculated by the weights of LiBr in the LBC-G cathodes in the low-potential plateau (<4.25 V; Fig. 2e, Extended Data Fig. 5a) at a low rate of ≤0.2 C (5-h charge/discharge) is very close to the theoretical redox capacity of LiBr (309 mAh g^{-1}), whereas that of the high-potential charging plateaus (>4.25 V), when calculated using the weights of LiCl, is close to the theoretical redox capacity of LiCl (632 mAh g^{-1}; Fig. 2f). Interestingly, the Coulombic efficiency of the LBC-G cathodes in the high-voltage plateau increases with increasing LiBr/LiCl ratio, which implies that the single intercalation of Cl^0 in graphite is thermodynamically forbidden at room temperature[20], unless it is paired with a Br^0. In sharp contrast, neat $(LiBr)_{0.5}(LiCl)_{0.5}$ in the absence of graphite could deliver a high oxidation capacity during the initial charging, but its discharge capacity is very low owing to the

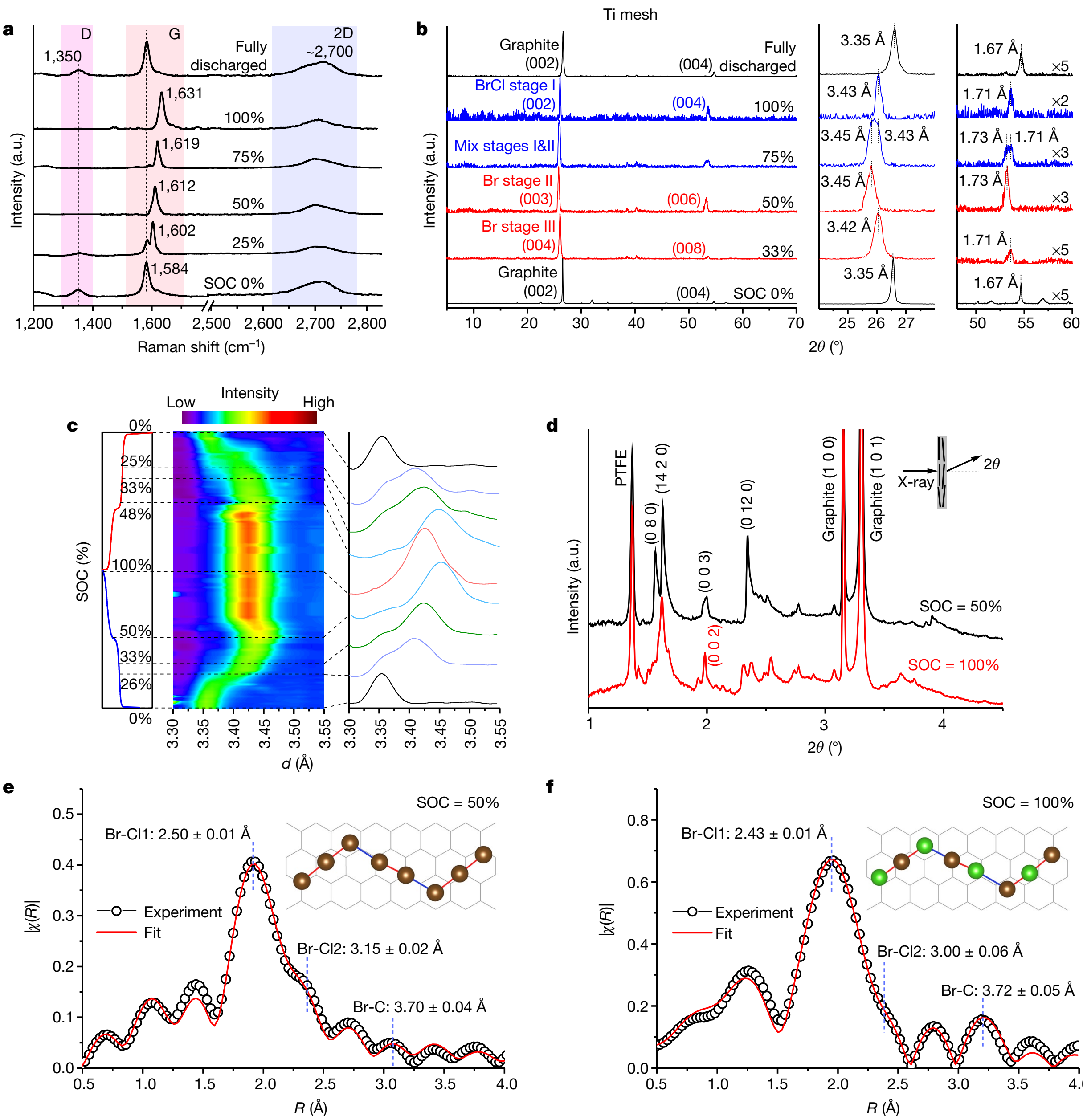

Fig. 3 | Staging structure and in-plane configurations of halogen GICs. a, Raman spectra (1,200–2,850 cm^{-1}) of LBC-G obtained in situ during the entire charge–discharge cycle, showing the graphite structure evolution with Br_2 and BrCl intercalation/de-intercalation. a.u., arbitrary units. The shaded regions indicate the featured carbon Raman bands, D, G and 2D. **b**, XRD spectra of the LBC-G composite obtained ex situ in various charging and discharging states through the second cycle. The θ–2θ scan mode (θ, diffraction angle) was employed with Cu Kα radiation (1.5418 Å) in reflection geometry. Left, full spectra. Middle, magnified spectra in the range $2\theta = 24°$–$28°$. Right, magnified spectra in the range $2\theta = 48°$–$60°$. The peaks of titanium current collectors were used to calibrate the displacement error. **c**, XRD patterns of the (0 0 m+1) peak of the LBC-G composite obtained in situ during a charge–discharge cycle. The patterns were collected with high-energy X-ray radiation (wavelength of 0.1173 Å) in transmission geometry. Left, corresponding voltage profile. Right, two-dimensional contour of XRD patterns and representative curves illustrating the continuous evolution of d spacing (3.30–3.55 Å) for the graphite host during intercalation/de-intercalation. The 2θ diffraction angles were converted to d spacing for convenience (see Methods). **d**, High-energy XRD patterns of LBC-G composites (electrolyte and current collector removed) at 50% and 100% SOC, acquired ex situ. High-energy transmission X-ray radiation (0.1173 Å) was applied perpendicular to most of the graphite flakes to reveal in-plane structure features. **e**, **f**, The best-fit modes for Br EXAFS experimental data of stage-II $C_7[Br]$ (**e**; SOC = 50%) and stage-I $C_{3.5}[Br_{0.5}Cl_{0.5}]$ (**f**; SOC = 100%). The EXAFS spectra are phase-uncorrected in R space, so the distances R in the two plots for the two stages are not comparable, but are both smaller than the actual values. Insets, in-plane configurations of stage-II $C_7[Br]$ and stage-I $C_{3.5}[Br_{0.5}Cl_{0.5}]$, obtained from DFT simulations. Two sets of bond distances are marked: short (red lines) and long (blue lines).

loss of gaseous halogens (Extended Data Fig. 5b). The carbon host can improve the reversibility of reactions by adsorbing halogens on its surface (Extended Data Fig. 5c), whereas the Coulombic efficiency improves with the graphitization degree of carbon hosts (Extended Data Fig. 5d–h), suggesting that graphitic materials provide a host structure that can reversibly accommodate halogen oxidation products.

The structural evolution of the graphite super-lattice was revealed using in situ Raman spectroscopy (1,200–2,850 cm^{-1}) during halogen intercalation (Fig. 3a)[21]. Upon halogen intercalation, the graphite G band (1,584 cm^{-1}) diminishes and gradually evolves into a feature corresponding to a stage-II GIC structure at 50% SOC, whereas at 100% SOC the peak further shifts to 1,631 cm^{-1}, indicating a stage-I GIC

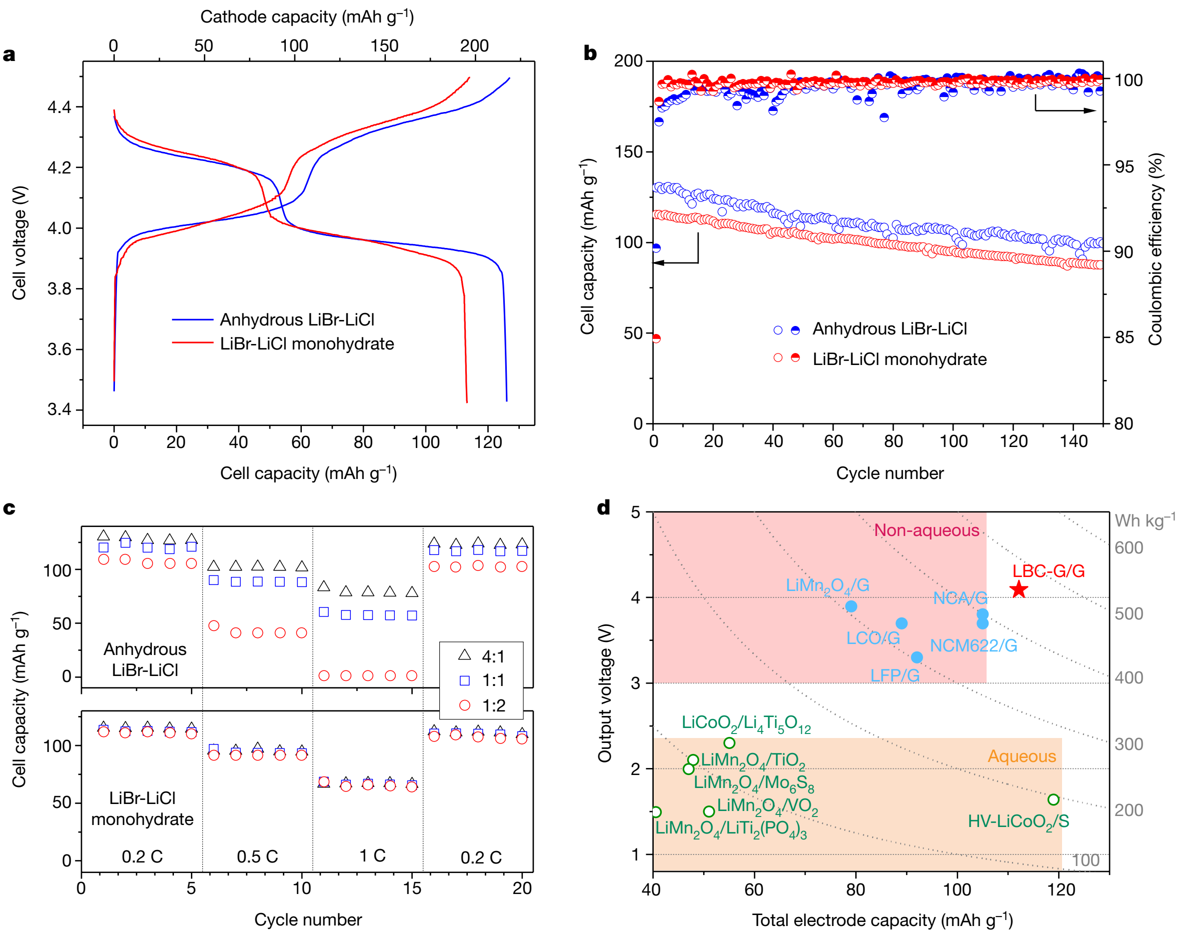

Fig. 4 | High-energy-density aqueous LIBs with LBC-G cathodes. **a**, Typical charge–discharge voltage profiles (third cycles) of two Li-ion full cells with LBC-G cathodes consisting of anhydrous LiBr/LiCl (blue) or LiBr/LiCl monohydrates (red) and HFE/poly(ethylene oxide)-protected graphite anodes. Charging and discharging were performed at 0.2 C (44 mA g^{-1} for the LBC-G cathode) at 25 °C. The cell capacity was calculated on the basis of the cathode mass alone (top horizontal axis) or the total mass of the cathode and the anode, including the binder and protective coating (bottom horizontal axis). **b**, Discharge capacities (using the total mass of the cathode and anode; open circles) and Coulombic efficiencies (semi-solid circles) of these full cells during cycling. **c**, Discharge capacities calculated using the total anode and cathode mass at various rates for LBC-G/graphite full cells with different electrolyte/electrodes (cathode and anode) mass ratios. **d**, Actual (red star) energy density of the LBC-G full cells (with LiBr/LiCl monohydrates), compared with various state-of-the-art commercial and experimental Li-ion chemistries using both non-aqueous (blue circles) and aqueous (green circles) electrolytes. For comparison, all energy densities were converted using the total weight of the positive and negative electrodes (not counting the electrolyte and cell packaging).

structure[22,23]. Upon discharging, a fully reversible change is observed in the Raman spectra. More details on the evolution of the staging structure were revealed in X-ray diffraction (XRD) spectra obtained ex situ. The LBC-G cathode (reflection geometry; Fig. 3b) shows a shifting dominant peak of (0 0 m+1) and a subdominant peak of (0 0 2m+2) during halogen intercalation/de-intercalation, verified by the reference patterns (Extended Data Fig. 6a, f) and the literature[24]. According to the well-reported intercalant gallery heights (7.00 Å for Br_2 and 6.85 Å for BrCl)[25,26], an accurate d spacing can be calculated for different GIC stage numbers m (Extended Data Table 1; calculation details in Methods). Close examination suggested a successive progression of d spacing for the dominant peak from 3.35 Å for pristine graphite (0 0 2), to $d_{003} \approx 3.45$ Å for stage-II Br_2-GIC at SOC of 0%–50%. Because the intercalant gallery height was slightly lower, further intercalation of Cl caused gradual shrinking of the d spacing, eventually reaching stage-I BrCl-GIC ($d_{002} \approx 3.43$ Å) at 100% SOC. In situ XRD of LBC-G (Fig. 3c) showed that the d spacing of (0 0 m+1) experienced continuous shifting during charging, indicating the gradual expansion of graphite interlayers when accommodating halogens[20]. A complete reversal of the above progression was again observed upon discharging, indicating a full recovery of the graphitic structure in a complete cycle.

The in-plane configuration and coordination of halogen intercalants in graphite provide knowledge that is necessary to determine the optimum intercalation concentration of this cathode chemistry. Because such structure is independent of the overall intercalate concentration, the stoichiometry n of C_n[Br] and C_n[BrCl] always remains the same in each intercalation domain[20]. Ex situ high-energy XRD (perpendicular incidence) for LBC-G at 50% and 100% SOC (Fig. 3d) showed multiple asymmetric and overlapping peaks, revealing mild long-range ordering of intercalant in-plane configurations. At 50% SOC, only three peaks in low diffraction angles can be indexed according to the single-crystal Br_2-GIC reference[27], indicating multi-phase coexistence, localized disorder and structure strain. DFT simulations based on two stoichiometries with n equal to integer multiples of 7 and 8 (Extended Data Fig. 7) yield zig-zag polymeric-like chains of –Br–Br– or –Br–Cl– with nearest in-plane distance of 2.4–3.2 Å (Fig. 3e, f, insets). All these configurations have similar potentials (within 20 mV), indicating that the real materials might be slightly disordered owing to the coexistence of these idealized model structures[28], in accordance with ex situ XRD patterns (Fig. 3d). MD simulations (Extended Data Fig. 8) predict that close Br–Br contacts may serve as hotspots for interconversion between different phases.

By fitting Br spectra acquired by extended X-ray absorption fine structure (EXAFS) measurements of LBC-G at 50% and 100% SOC (Fig. 3e, f), the most compatible models were C_{7m}[BrBr] and C_{7m}[BrCl], both with two sets of the nearest in-plane distances (Br-X1 and

Br-X2, X = Br or Cl) instead of consistent distances for C_{8m}[BrBr] and C_{8m}[BrCl] (Extended Data Fig. 9). Because of the interaction of graphene planes with π electrons, the average nearest in-plane distances of halogen intercalants were 2.50 Å for Br-Br1, 3.15 Å for Br-Br2, 2.43 Å for Br-Cl1 and 3.00 Å for Br-Cl2, somewhat longer than the bond lengths in free Br_2 (about 2.30 Å) and BrCl (2.18 Å) molecules. However, these nearest in-plane distances are much shorter than those of alkali-metal GICs (4.30–4.92 Å) and large-anion GICs (8–10 Å)[29], which means that the halogen intercalants possess one of the highest in-plane densities among all GICs reported. This high-density packing is mainly due to the near-zero oxidation valence of halogen intercalates, which generates much lower Coulomb repulsion from average effective charge of about −0.16 per halogen atom (Fig. 2d), compared with about +0.90 for Li-GIC[30] and −1 for complex anions.

Aqueous lithium-ion battery (LIB) full cells were constructed using an aqueous gel electrolyte derived from a WiBS[4] and LBC-G cathode coupled with a graphite anode protected by a highly fluorinated ether (HFE) polymer gel[2], which was developed earlier for 4-V aqueous LIB (cell configuration in Extended Data Fig. 4d, e). A stable discharge capacity of 127 mAh g^{-1} (total anode/cathode mass) was obtained at an average voltage of 4.1 V at 0.2 C (Fig. 4a), and 74% of this initial capacity was retained over 150 cycles at an average Coulombic efficiency of 99.8% (Fig. 4b). The low self-discharge rate (Extended Data Fig. 2f) demonstrated that the super-concentrated aqueous gel electrolyte effectively suppressed parasitic reactions, especially water decomposition and loss of halogen active material from the cathode.

Because the formation of a hydrated LiBr/LiCl layer via extraction of water from WiBS is critical for achieving high power density, the WiBS/cathode mass ratio affects the rate performance. The rate capability was severely compromised when the electrolyte/electrodes mass ratio was reduced from 4:1 to 1:2 (Fig. 4c). However, a high WiBS/cathode ratio is not desired either, because it reduces the energy density. As a simple solution to this dilemma, the anhydrous salts were replaced by their monohydrate forms ($LiBr \cdot H_2O$/$LiCl \cdot H_2O$; Extended Data Fig. 1b), resulting in almost identical charge/discharge profiles (Fig. 4a, b). The rate capability of such full cells is much better, while the impact of the electrolyte/electrodes mass ratio is minimized. Given that battery performances constructed with LiBr/LiCl monohydrates are independent of the electrolyte amount, we estimated the energy density of such aqueous LIBs to be around 460 Wh kg^{-1} (total mass of cathode and anode). This energy density is greater than that of state-of-the-art non-aqueous LIBs (Fig. 4d). After considering the electrolyte mass, the full-cell energy density still reaches 304 Wh kg^{-1}. Importantly, this high energy density comes with intrinsic safety and environmental insensitivity, brought by its aqueous nature. The proposed conversion–intercalation aqueous cathode chemistry offers an energy-dense concept for a future battery that is cost-effective, safe and flexible.

Online content

Any methods, additional references, Nature Research reporting summaries, source data, statements of data availability and associated accession codes are available at https://doi.org/10.1038/s41586-019-1175-6.

Received: 27 April 2018; Accepted: 23 February 2019;
Published online 8 May 2019.

1. Suo, L. et al. "Water-in-salt" electrolyte enables high-voltage aqueous lithium-ion chemistries. *Science* **350**, 938–943 (2015).
2. Yang, C. et al. 4.0 V aqueous Li-ion batteries. *Joule* **1**, 122–132 (2017).
3. Suo, L. et al. Advanced high-voltage aqueous lithium-ion battery enabled by "water-in-bisalt" electrolyte. *Angew. Chem. Int. Ed.* **55**, 7136–7141 (2016).
4. Yang, C. et al. Unique aqueous Li-ion/sulfur chemistry with high energy density and reversibility. *Proc. Natl Acad. Sci. USA* **114**, 6197–6202 (2017).
5. Larcher, D. & Tarascon, J. M. Towards greener and more sustainable batteries for electrical energy storage. *Nat. Chem.* **7**, 19–29 (2015).
6. Radin, M. D. et al. Narrowing the gap between theoretical and practical capacities in Li-ion layered oxide cathode materials. *Adv. Energy Mater.* **7**, 1602888 (2017).
7. Zhan, C. et al. Enabling the high capacity of lithium-rich anti-fluorite lithium iron oxide by simultaneous anionic and cationic redox. *Nat. Energy* **2**, 963–971 (2017).
8. Lee, J. et al. Reversible Mn^{2+}/Mn^{4+} double redox in lithium-excess cathode materials. *Nature* **556**, 185–190 (2018).
9. Bruce, P. G., Freunberger, S. A., Hardwick, L. J. & Tarascon, J. M. Li-O_2 and Li-S batteries with high energy storage. *Nat. Mater.* **11**, 19–29 (2012); erratum **11**, 172 (2012).
10. Seel, J. A. & Dahn, J. R. Electrochemical intercalation of PF_6 into graphite. *J. Electrochem. Soc.* **147**, 892–898 (2000).
11. Milliken, J. W. & Fischer, J. E. Ionic salt limit in graphite–fluoroarsenate intercalation compounds. *J. Chem. Phys.* **78**, 5800–5808 (1983).
12. Wu, F. & Yushin, G. Conversion cathodes for rechargeable lithium and lithium-ion batteries. *Energy Environ. Sci.* **10**, 435–459 (2017).
13. Axdal, S. H. A. & Chung, D. D. L. Kinetics and thermodynamics of intercalation of bromine in graphite—I. Experimental. *Carbon* **25**, 191–210 (1987).
14. Erbil, A., Dresselhaus, G. & Dresselhaus, M. S. Raman scattering as a probe of structural phase transitions in the intercalated graphite–bromine system. *Phys. Rev. B* **25**, 5451–5460 (1982).
15. Anthonsen, J. The Raman spectra of some halogen gas hydrates. *Acta Chem. Scand. A* **29a**, 175–178 (1975).
16. Stammreich, H. & Forneris, R. The Raman frequency of bromine monochloride. *J. Chem. Phys.* **21**, 944–945 (1953).
17. Heald, S. M. & Stern, E. A. Extended-x-ray-absorption-fine-structure study of the Br_2-graphite system. *Phys. Rev. B* **17**, 4069–4081 (1978).
18. Huggins, F. E. & Huffman, G. P. Chlorine in coal: an XAFS spectroscopic investigation. *Fuel* **74**, 556–569 (1995).
19. Heald, S. M. & Stern, E. A. EXAFS study of Br_2-graphite intercalation compounds. *Synth. Met.* **1**, 249–255 (1980).
20. Selig, H. & Ebert, L. B. Graphite intercalation compounds. *Adv. Inorg. Chem. Radiochem.* **23**, 281–327 (1980).
21. Dresselhaus, M. S. & Dresselhaus, G. Intercalation compounds of graphite. *Adv. Phys.* **30**, 139–326 (1981).
22. Cao, J. et al. Two-step electrochemical intercalation and oxidation of graphite for the mass production of graphene oxide. *J. Am. Chem. Soc.* **139**, 17446–17456 (2017).
23. Lin, M. C. et al. An ultrafast rechargeable aluminium-ion battery. *Nature* **520**, 324–328 (2015).
24. Leung, S. Y. et al. Structural studies of graphite intercalation compounds using (00*l*) x-ray diffraction. *Phys. Rev. B* **24**, 3505–3518 (1981).
25. Furdin, G., Bach, B. & Herold, A. Contribution à l'étude du système ternaire graphite–brome–chlore. *C. R. Acad. Sci. Paris C* **271**, 683 (1970).
26. Eeles, W. & Turnbull, J. The crystal structure of graphite-bromine compounds. *Proc. R. Soc. Lond. A* **283**, 179–193 (1965).
27. Sasa, T., Takahashi, Y. & Mukaibo, T. Crystal structure of graphite bromine lamellar compounds. *Carbon* **9**, 407–416 (1971).
28. Chung, D. Structure and phase transitions of graphite intercalated with bromine. *Phase Transit.* **8**, 35–57 (1986).
29. Placke, T. et al. In situ X-ray diffraction studies of cation and anion intercalation into graphitic carbons for electrochemical energy storage applications. *Z. Anorg. Allg. Chem.* **640**, 1996–2006 (2014).
30. Titantah, J. T., Lamoen, D., Schowalter, M. & Rosenauer, A. Density-functional theory calculations of the electron energy-loss near-edge structure of Li-intercalated graphite. *Carbon* **47**, 2501–2510 (2009).

Acknowledgements The principal investigators (C.W. and K.X.) received financial support from the US Department of Energy (DOE) through ARPA-E grant DEAR0000389. O.B. and T.P. acknowledge support from ARL Enterprise for Multiscale Modelling. This research used resources of the Advanced Photon Source, an Office of Science User Facility operated for the US DOE Office of Science by Argonne National Laboratory, and was supported by the US DOE under contract number DE-AC02-06CH11357 and by the Canadian Light Source and its funding partners.

Reviewer information *Nature* thanks Chao Gao, Jintao Zhang and the other anonymous reviewer(s) for their contribution to the peer review of this work.

Author contributions C.Y., J.C. and C.W. conceived the idea of the study. C.Y., J.C., S.H. and T.Q. prepared the materials and performed electrochemical experiments. X.J., O.B. and T.P.P. conducted DFT and MD simulations. C.Y. and J.C. conducted Raman spectroscopy measurements. C.Y., X.L., Q.L. and Y.R. performed X-ray diffraction measurements. C.Y., Y.W., C.L. and C.-J.S. performed X-ray absorption spectroscopy measurements. C.Y., K.X. and C.W. wrote the paper, and all authors contributed to editing the manuscript.

Competing interests The authors declare no competing interests.

Additional information
Extended data is available for this paper at https://doi.org/10.1038/s41586-019-1175-6.
Reprints and permissions information is available at http://www.nature.com/reprints.
Correspondence and requests for materials should be addressed to C.W.
Publisher's note: Springer Nature remains neutral with regard to jurisdictional claims in published maps and institutional affiliations.

METHODS

Preparation of electrodes. For the three-electrode cells, LBC-G composite was obtained by homogenously mixing anhydrous LiBr (99.9%; Sigma-Aldrich), LiCl (99.9%; Sigma-Aldrich) and synthetic graphite powder (TIMCAL TIMREX KS4; average particle size of about 4.1 μm) by zirconia ball milling for 15 min. The LiBr:LiCl molar ratio was 1:1, whereas the LiBr:LiCl:graphite mass ratio was about 2:1:2. In the full cells with LiBr/LiCl monohydrates, all the procedures were the same, except that anhydrous LiBr/LiCl was replaced by $LiBr{\cdot}H_2O$ (99.95%; Sigma-Aldrich) and LiCl (99.95%; Sigma-Aldrich). Other control samples were obtained by adjusting the composites to the following mass ratios: LiBr:LiCl:titanium nanopowder, about 2:1:60 for $(LiBr)_{0.5}(LiCl)_{0.5}$-Ti; LiBr:LiCl:active carbon, about 2:1:9 for $(LiBr)_{0.5}(LiCl)_{0.5}$-AC; LiBr:LiCl:graphited acetylene black, about 2:1:9 for $(LiBr)_{0.5}(LiCl)_{0.5}$-CB. Composite LBC-G cathodes were fabricated by compressing LBC-G composite and polytetrafluoroethylene (PTFE; Sigma-Aldrich) at a weight ratio of 95:5 on a titanium metal mesh (Alfa Aesar; 100 mesh). The areal loading of the cathode material was about 38 mg cm^{-2}. The thickness of the cathode was about 200 μm. The graphite anodes were fabricated using mesocarbon microbead graphite powder (MTI Corp.) and PTFE at a weight ratio of 9:1 on a stainless steel mesh (200 mesh).

Preparation of electrolytes. The liquid WiBS aqueous electrolytes were first prepared by dissolving 21 mol kg^{-1} LiTFSI (>98%; TCI Co. Ltd) and 7 mol kg^{-1} lithium trifluoromethanesulfonate (LiOTf; 99.995%; Sigma-Aldrich) in water (HPLC grade). Aqueous gel electrolytes were prepared by mixing 20 wt% poly(ethylene oxide) (PEO; viscosity-average molecular weight, $M_v \approx 600{,}000$; Sigma-Aldrich) or 10 wt% polyvinyl alcohol (weight-average molecule weight, $M_w = 146{,}000$–$186{,}000$; >99% hydrolysed; Sigma-Aldrich) with WiBS electrolyte and heated at 80 °C for 1 h in sealed glass moulds. After cooling to room temperature, sticky semi-solid WiBS gel electrolytes were obtained, which could be changed into any shape at 50 °C. The preparation of HFE-PEO gel protection coating has been reported previously[2]. Briefly, the coating gel is prepared by mixing 1,1,2,2-tetrafluoroethyl-2′,2′,2′-trifluoroethyl ether (Daikin America or Apollo) with 0.5 M LiTFSI (denoted as LiTFSI-HFE gel) and 10 wt% PEO in HFE/fluoroethylene carbonate (with volume ratio 95:5) and heated at 70 °C for 5 min under vigorous stirring.

Preparation of chemical GICs as reference samples. Reference samples of chemically intercalated Br_2 and BrCl GICs were synthesized following a previously reported procedure[19,25]. Briefly, Br_2 and BrCl GICs were prepared by exposing the graphite flakes (TIMCAL TIMREX KS4) in high-concentration Br_2 vapour (99.99%; Sigma-Aldrich) and BrCl gas in well-sealed flasks for 2 h. BrCl was prepared by mixing Br_2 with an equimolar quantity of Cl_2, which was obtained from the reaction of trichloroisocyanuric acid and hydrochloric acid, at −70 °C. The as-prepared GICs were immediately transferred to the Raman or XRD measurement systems to avoid slow de-intercalation after being removed from the halogen gas atmosphere and exposed to air.

Electrochemical measurements. In the three-electrode cells, the LBC-G electrodes (or other control electrodes) were used as the working electrode, active carbon as the counter-electrode and Ag/AgCl as the reference electrode. The mass ratio of the working electrode versus the electrolyte was 1:20. The three-electrode cells were then galvanostatically charged/discharged using a Land BT2000 battery test system (Wuhan, China) at room temperature. Cyclic voltammetry was carried out using a CHI 600E electrochemical work station. The GITT experiment was performed using a three-electrode device with the same electrode configuration. The cycling protocol consisted of current pulses of 80 mA g^{-1} (0.2 C) for 20 min alternated with 120-min open-circuit-voltage periods to reach quasi-equilibrium potentials. The apparent ionic diffusion coefficients (D) of the reactants in the LBC-G cathode at different states of charge and discharge were estimated from the GITT measurement using the following relation[31]:

$$D = \frac{4}{\pi}\left(\frac{IV_{\mathrm{m}}}{FS}\right)^2 \left(\frac{\mathrm{d}E/\mathrm{d}x}{\mathrm{d}E/\mathrm{d}(t^{1/2})}\right)^2 \tag{3}$$

where I is the applied constant current density, V_{m} is the molar volume of partially hydrated LiBr/LiCl, F is the Faraday constant (96,486 C mol^{-1}), S is the contact area between the electrolyte and the active materials, $\mathrm{d}E/\mathrm{d}x$ is the slope of the Coulometric titration curve at composition x, and $\mathrm{d}E/\mathrm{d}(t^{1/2})$ can be obtained from the plot of the transient voltage versus the square root of time during constant current pulses. The four-point EIS measurement was performed with a Gamry 345 interface 1000 using a 5-mV perturbation with frequency in the range 0.01–100,000 Hz at room temperature. The ionic diffusion coefficient was calculated by simulation, using an equivalent circuit including a finite Warburg element[32].

The full cells were assembled as CR2032-type coin cells using LBC-G as the cathode and HFE-PEO-gel-protected graphite electrodes as the anode. The cathode/anode mass ratios were 1.38:1. A titanium metal foil disk was placed between the cathode and the coin cell case to prevent corrosion. As-prepared WiBS gel electrolyte was pressed into films and applied in the coin cells as both electrolyte and separator. The ratio of the total mass of the electrodes to that of the electrolyte was from 1:4 to 2:1. After assembly, the cell was briefly kept at 50 °C for gel polymer electrolyte self-healing. The full cell was then cycled galvanostatically on a Land BT2000 battery test system (Wuhan, China) at room temperature.

The specific (gravimetric or volumetric) energy densities (E) of the full cells were calculated by

$$E = CU \tag{4}$$

where C is the specific (gravimetric or volumetric) cell capacity and U is the average cell output voltage. The gravimetric capacity C_m was calculated by

$$C_m = \frac{C_{\mathrm{cell}}}{m_{\mathrm{cathode}} + m_{\mathrm{anode}}} \tag{5}$$

where C_{cell} is the absolute cell capacity; m_{cathode} is the total mass of the cathode, including LiBr, LiCl, graphite and PTFE binder; and m_{anode} is the total mass of the anode, including graphite, PTFE binder and the polymer passivation coating.

In situ Raman spectroscopy. For the in situ Raman measurements, a LBC-G/G full cell (in a coin cell configuration) was charged and discharged at 40 mA g^{-1} (0.1 C). A quartz optical window (diameter $\phi = 5$ mm) was applied on the cathode side. Raman spectra were collected with a Horiba Jobin Yvon Labram Aramis Raman spectrometer using a laser (wavelength of 532 nm) at frequencies between 3,500 cm^{-1} and 60 cm^{-1}. 16 data points per sample were collected to get a high signal-to-noise ratio.

Ex situ and in situ XRD spectroscopy. For the ex situ XRD measurements, the LBC-G electrodes (working electrodes) were retracted from the three-electrode cell after being charged/discharged to certain SOCs at 40 mA g^{-1} (0.1 C). For the in situ XRD study, a full cell (in a coin cell configuration) was charged and discharged at 0.1 C. Kapton windows ($\phi = 3$ mm) were used on both sides of the coin cells, where the anode was placed to avoid beam passage through the window. XRD patterns (Fig. 3b) were recorded ex situ on a Bruker D8 Advance XRD system with Cu Kα radiation in grazing-incidence geometry. High-energy synchrotron XRD measurements (Fig. 3c, d) were carried out at the 11-ID-C beamline of the Advanced Photon Source (APS), Argonne National Laboratory. A high-energy X-ray with beam size 0.2 mm × 0.2 mm and wavelength 0.1173 Å was used to obtain two-dimensional diffraction patterns in the transmission geometry. X-ray patterns were recorded with a Perkin-Elmer large-area detector placed at 1,800 mm from the battery cells. The interval between successive diffraction measurements was 5 min. The obtained two-dimensional diffraction patterns were calibrated using a standard CeO_2 sample and converted to one-dimensional patterns using Fit2D software.

The periodic repeat distance (I_{C}) and the intercalant gallery height (d_i) of the GICs can be calculated using[23]

$$I_{\mathrm{C}} = d_i + (3.35\ \text{Å}) \times (m-1) = l \times d_{\mathrm{obs}} \tag{6}$$

where l is the index of the (0 0 l) planes oriented in the stacking direction and d_{obs} is the observed value of the spacing between two adjacent planes in the XRD patterns, which can be calculated from the diffraction angles by Bragg's law. The d spacing of pristine graphite is 3.35 Å. The intensity pattern was usually found for a stage-m GIC, where the most dominant peak is the (0 0 m+1). The d spacing values of (0 0 m+1) were calculated from the XRD data using Bragg's law (Extended Data Table 1), and the most dominant stage phase of the observed GIC was assigned.

Ex situ XANES and EXAFS studies. Ex situ X-ray absorption spectroscopy measurements were conducted on the same cell configuration as that used for the in situ XRD measurements. The experiments were carried out in transmission mode at the beamline 20-BM-B of APS. The XANES measurements were performed at the K edge of bromine (about 13,474 eV) and chlorine (about 2,822 eV) to monitor the change of the valence state of Br and Cl in the cathode, and the energy calibration was performed using the first-derivative point of the XANES spectrum of Bi (L_{III} edge; 13,419 eV). During the Cl measurement, the entire X-ray beam, samples and detector were protected by helium gas. The reference spectra were collected for each spectrum by placing the bismuth metal foil in the reference channel. The EXAFS spectra were aligned, merged and normalized using Athena[33,34]. The coin cells were charged to certain voltages with a constant current before the measurements.

The Athena program was first used to process experimental X-ray absorption data to extract the normalized oscillation amplitude $\chi^{\exp}(k)$, where the photoelectron wavenumber k is defined by $k = \sqrt{2m(E-E_0)}/\hbar$, where E_0 is the absorption edge energy and $\hbar$ is the reduced Planck constant. The theoretically calculated $\chi^{\mathrm{th}}(k)$ is given by the EXAFS equation[35]

$$\chi^{\mathrm{th}}(k) = \sum_j \frac{S_0^2 N_j f_j(k)}{kR_j^2} \mathrm{e}^{-2k^2\sigma_j^2} \mathrm{e}^{-2r_j/\lambda(k)} \sin[2kR_j + \delta_j(k, r_j)] \tag{7}$$

where j indicates the jth atomic shell including the atoms with identical distance to the central atom, N_j is the coordination number of the jth shell, f_j is the back-scattering amplitude, R_j is the average distance between the central atom and back-scatters, σ_j is the mean square variation in R_j, δ_j is the scattering phase shift, λ is the effective mean free path and S_0^2 is the amplitude reduction factor. FEFF6 was used to calculate f_j, δ_j and λ. Fitting of the experimental data was carried out using Artemis to refine the structure parameters S_0^2, N_j, R_j and σ_j^2. The initial crystal structures used in the fitting were DFT-optimized stage-II $C_7[Br]$ and stage-I $C_{3.5}[Br_{0.5}Cl_{0.5}]$. S_0^2 was fixed at 1.0. Two energy intervals ΔE were used in the fitting: one for the Br–Br (or Cl) paths and one for the remaining Br–C paths.

Phase separation and water equilibrium studies. For the water uptake estimation, WiBS liquid electrolyte was gradually (in 0.1-g steps) added into 20 mg of anhydrous LiBr/LiCl or LiBr/LiCl monohydrate mixed salts (20 mg; molar ratio, 1:1) during shake mixing for 2 h and 6 h of standing (each time), until no solid residue was observed. For the demonstration of phase separation, an as-prepared aqueous solution of $LiBr{\cdot}3H_2O$ (0.8 g) and $LiCl{\cdot}3H_2O$ (0.4 g) was added into the WiBS liquid electrolyte (3 g), following by 2 h of shake mixing and 1 h of standing. After 500 h of further exposure to LiCl/LiBr solution, a small sample of WiBS was removed and the Br^- and Cl^- concentration was tested by anion exchange liquid chromatography (Dionex ICS-1100 Ion Chromatography System).

Scanning electron microscopy imaging and specific-surface-area measurement. Scanning electron microscopy of the cycled cathode was performed using a Hitachi SU-70 microscope equipped with an energy-dispersive X-ray spectroscopy system operating at 5 kV. Specific surface areas of the samples were characterized by N_2 adsorption by means of a Micromeritics ASAP 2020 Porosimeter test station. The samples were degassed (in a vacuum) at 180 °C for 12 h before the test. The specific surface areas were calculated using the Brunauer–Emmett–Teller method from the adsorption branch.

MD simulations of LiBr in water-in-salt electrolyte. MD simulations were performed on 18 m (moles salt per kilogram of solvent) LiBr in water at 333 K and a mixed salt of 18 m LiBr and 21 m LiTFSI in water at 363 K. The MD simulations used a previously modified CHARMM H_2O force field[36] in conjunction with the APPLE&P many-body polarizable force field for LiTFSI in H_2O, which predicted the ionic conductivity, ion and water self-diffusion coefficients, as well as the viscosity and density of LiTFSI-H_2O, in excellent agreement with experiments[37] over a wide range of salt concentrations from 5 m to 21 m. The APPLE&P functional form and combining rules are given elsewhere[38].

A parallel version of the in-house-developed MD simulation package was used for MD simulations. The mixed-salt cell contained 1,380 H_2O, 512 LiTFSI and 448 LiBr molecules corresponding to 21 m LiTFSI and 18 m LiBr. The initial simulation cell had linear dimensions of 95 Å. The dimensions of the simulation box were gradually decreased to 60 Å. NPT (constant pressure and temperature) simulations were performed for 2 ns at 363 K for the mixed-salt system using a modified force field with increased repulsion between Br–Br and TFSI–TFSI anions to disperse them evenly in the simulation box as shown in Extended Data Fig. 1e (left). After 9 ns of MD simulations in the NPT ensemble, LiBr(H_2O) largely separated from the LiTFSI(H_2O) domain (right). Such behaviour is indicative of the initial stages of phase separation and is in accord with experimental observations.

The Ewald summation method was used in the MD simulations to handle the electrostatic interactions between permanent charges and between permanent charges and induced dipole moments using $k = 6^3$ vectors. Multiple timestep integration was employed with an inner timestep of 0.5 fs (bonded interactions), a central timestep of 1.5 fs for all nonbonded interactions within a truncation distance of 7.0–8.0 Å, and an outer timestep of 3.0 fs for all nonbonded interactions between 7.0 Å and the nonbonded truncation distance of 19 Å. The reciprocal part of the Ewald summation was updated only at the largest of the multiple timesteps. A Nose–Hoover thermostat and a barostat were used to control the temperature and pressure with frequencies of 10^{-2} fs and 0.1×10^{-4} fs, respectively. The atomic coordinates were saved every 2 ps for post-analysis.

The ability of MD simulations using an atomic dipole polarizable APPLE&P force field to predict density and conductivity of 18 m LiBr in H_2O was examined at 333 K. The simulation cell contained 448 LiBr and 1,390 H_2O molecules. After 3-ns equilibration in the NPT ensemble, 8-ns MD simulations in an NVT ensemble (constant volume) predicted an electrolyte density of 1,649 kg m^{-3}, which is 0.8% higher than the experimental density[39] of 1,636.5 kg m^{-3}. The ionic conductivity (σ) was extracted using the Einstein relations

$$\sigma = \lim_{t\to\infty}\frac{e^2}{6tVk_BT}\sum_{i,j}^{N} z_i z_j\left\langle\{[\boldsymbol{R}_i(t)-\boldsymbol{R}_i(0)]\}\cdot\{[\boldsymbol{R}_j(t)-\boldsymbol{R}_j(0)]\}\right\rangle \quad (8)$$

where V is the volume of the simulation box, k_B is Boltzmann's constant, T is the temperature, t is the time, z_i and z_j are the Li^+ and Br^- charges, $R_i(t)$ is the displacement of ion i during time t, the angle brackets denote the ensemble average and N is the diffusion number. Owing to the finite size of the simulation cell, long-range hydrodynamic interactions restrict diffusion. The leading-order finite-size correction (FSC)[38,40] to the self-diffusion coefficient is given by

$$\Delta D^{\mathrm{FSC}} = \frac{2.837k_BT}{6\pi\eta L} \quad (9)$$

where L is a linear dimension of the simulation periodic cell and η is the viscosity. After the FSC correction, MD simulations predicted the conductivity of the 18 m LiBr electrolyte to be 75 mS cm^{-1}, which is 30% lower than the experimentally determined conductivity of 98.89 mS cm^{-1} but is sufficiently accurate for the highly concentrated electrolyte prediction.

DFT simulations of intercalation structure configuration. All calculations were performed using DFT simulations with a plane-wave basis set and the projector augmented wave[41] method, as implemented in the Vienna ab initio simulation package (VASP)[42]. The Perdew–Burke–Ernzerhof (PBE) functional in the generalized gradient approximation[43] was employed to calculate the exchange-correlation energy. An energy cutoff of 580 eV was used for the plane-wave basis, and the Brillouin zone was sampled using the Monkhorst–Pack scheme. The van der Waals density functional of optB86b[44] was used to correct the Van der Waals energies and obtain accurate interlayer spacing values in all cases. According to previous work, two sets of possible configurations for ($C_7[Br]$, $C_{3.5}[Br_{0.5}Cl_{0.5}]$) and ($C_8[Br]$, $C_4[Br_{0.5}Cl_{0.5}]$) were taken into consideration[26,45]. In these configurations the Br and Cl atoms were initialized randomly. The geometry optimizations were performed using the conjugated gradient method, and the convergence threshold was set to be 10^{-5} eV in energy and 0.01 eV Å^{-1} in force. The charge-difference plots were obtained by subtracting the charge density of both graphite and Br (BrCl) from the charge density of $C_7[Br]$ ($C_{3.5}[Br_{0.5}Cl_{0.5}]$), respectively. The charge distribution on the atoms was determined using the Bader analysis method[46]. Visualization of the structures was made using VESTA software[47].

Intercalation voltage step profile simulation. Intercalation voltage profiles were computed with CP2K v5.1[36] using the dispersion-corrected (D3)[48,49] PBE[50] functional and the DZVP-MOLOPT-SR-GTH basis set (TZVP-MOLOPT-SR-GTH for bromide)[51] and appropriate Goedecker–Teter–Hutter pseudopotentials[52,53] for core electrons. The plane-wave energy cutoff was set to 1,000 Ry and the Brillouin zone was sampled at the Γ point only. The geometry and cell optimizations converged to a maximum change in atomic positions between steps of 0.0005 atomic units. The other convergence criteria were left at their default values.

The intercalation voltage (E_{int}) against Li/Li$^+$ was computed from a series of energy calculations, assuming a negligible entropic contribution, as

$$E_{\mathrm{int}} = \frac{E(\mathrm{GX}) - E(\mathrm{G}) + n_X E_{\mathrm{desolv}}(\mathrm{LiX}) - n_X E_{\mathrm{gas}}(\mathrm{LiX}) + n_X E_b(\mathrm{Li})}{n_X} \quad (10)$$

Above, n_X is the number of anions, E(GX) is the energy of the intercalated graphite gallery, E(G) the energy of pure graphite in AB stacking, E_{desolv}(LiX) the desolvation energy of a LiX contact ion pair, calculated using the cluster-continuum method (with up to eight explicit water molecules) and Gaussian09 A.1[54] calculations with PBEPBE+D3/6-31G(d)[43,48,49,55], E_{gas}(LiX) the energy of the LiX contact ion pair in a $10 \times 10 \times 10$ Å^3 cell and E_b(Li) the energy per Li atom in the bulk metal (−204.1894 eV per Li atom). For stages I–IV, VI, 12 layers of carbon were modelled. Stage V was modelled with 10 layers of carbon. Each layer consisted of 112 carbon atoms.

Data availability

The data that support the findings of this study are available from the corresponding author on request.

31. Wen, C. J., Boukamp, B. A., Huggins, R. A. & Weppner, W. Thermodynamic and mass transport properties of "LiAl". *J. Electrochem. Soc.* **126**, 2258–2266 (1979).
32. Barsoukov, E. & Macdonald, J. R. *Impedance Spectroscopy: Theory, Experiment, and Applications* (John Wiley & Sons, Hoboken, 2018).
33. Ravel, B. & Newville, M. ATHENA, ARTEMIS, HEPHAESTUS: data analysis for X-ray absorption spectroscopy using IFEFFIT. *J. Synchrotron Radiat.* **12**, 537–541 (2005).
34. Newville, M. EXAFS analysis using FEFF and FEFFIT. *J. Synchrotron Radiat.* **8**, 96–100 (2001).
35. Bunker, G. *Introduction to XAFS: A Practical Guide to X-ray Absorption Fine Structure Spectroscopy* (Cambridge Univ. Press, Cambridge, 2010).
36. Starovoytov, O. N., Borodin, O., Bedrov, D., & Smith, G. D. Development of a polarizable force field for molecular dynamics simulations of poly (ethylene oxide) in aqueous solution. *J. Chem. Theory Comput.* **7**, 1902–1915 (2011).
37. Borodin, O. et al. Liquid structure with nano-heterogeneity promotes cationic transport in concentrated electrolytes. *ACS Nano* **11**, 10462–10471 (2017).
38. Borodin, O. Polarizable force field development and molecular dynamics simulations of ionic liquids. *J. Phys. Chem. B* **113**, 11463–11478 (2009).

39. Zaytsev, I. D. & Aseyev, G. G. *Properties of Aqueous Solutions of Electrolytes*. (CRC Press, Boca Raton, 1992).
40. Dünweg, B. & Kremer, K. Molecular dynamics simulation of a polymer chain in solution. *J. Chem. Phys*. **99**, 6983–6997 (1993).
41. Blöchl, P. E. Projector augmented-wave method. *Phys. Rev. B* **50**, 17953 (1994).
42. Kresse, G. & Hafner, J. Ab initio molecular-dynamics simulation of the liquid-metal–amorphous-semiconductor transition in germanium. *Phys. Rev. B* **49**, 14251 (1994).
43. Perdew, J. P., Burke, K. & Ernzerhof, M. Generalized gradient approximation made simple. *Phys. Rev. Lett*. **77**, 3865 (1996).
44. Klimeš, J., Bowler, D. R. & Michaelides, A. Chemical accuracy for the van der Waals density functional. *J. Phys. Condens. Matter* **22**, 022201 (2009).
45. Ghosh, D. & Chung, D. D. L. Two-dimensional structure of bromine intercalated graphite. *Mater. Res. Bull*. **18**, 1179–1187 (1983).
46. Henkelman, G., Arnaldsson, A. & Jónsson, H. A fast and robust algorithm for Bader decomposition of charge density. *Comput. Mater. Sci*. **36**, 354–360 (2006).
47. Momma, K. & Izumi, F. VESTA 3 for three-dimensional visualization of crystal, volumetric and morphology data. *J. Appl. Cryst*. **44**, 1272–1276 (2011).
48. Grimme, S., Antony, J., Ehrlich, S. & Krieg, H. A consistent and accurate ab initio parametrization of density functional dispersion correction (DFT-D) for the 94 elements H–Pu. *J. Chem. Phys*. **132**, 154104 (2010).
49. Grimme, S., Ehrlich, S. & Goerigk, L. Effect of the damping function in dispersion corrected density functional theory. *J. Comput. Chem*. **32**, 1456–1465 (2011).
50. Zhang, Y. & Yang, W. Comment on "Generalized gradient approximation made simple". *Phys. Rev. Lett*. **80**, 890 (1998).
51. VandeVondele, J. & Hutter, J. Gaussian basis sets for accurate calculations on molecular systems in gas and condensed phases. *J. Chem. Phys*. **127**, 114105 (2007).
52. Goedecker, S., Teter, M. & Hutter, J. Separable dual-space Gaussian pseudopotentials. *Phys. Rev. B* **54**, 1703–1710 (1996).
53. Hartwigsen, C., Gœdecker, S. & Hutter, J. Relativistic separable dual-space Gaussian pseudopotentials from H to Rn. *Phys. Rev. B* **58**, 3641 (1998).
54. Frisch, M. J. et al. *Gaussian 09, revision A. 1* http://gaussian.com/glossary/g09/ (2009).
55. Francl, M. M. et al. Self-consistent molecular orbital methods. XXIII. A polarization-type basis set for second-row elements. *J. Chem. Phys*. **77**, 3654–3665 (1982).

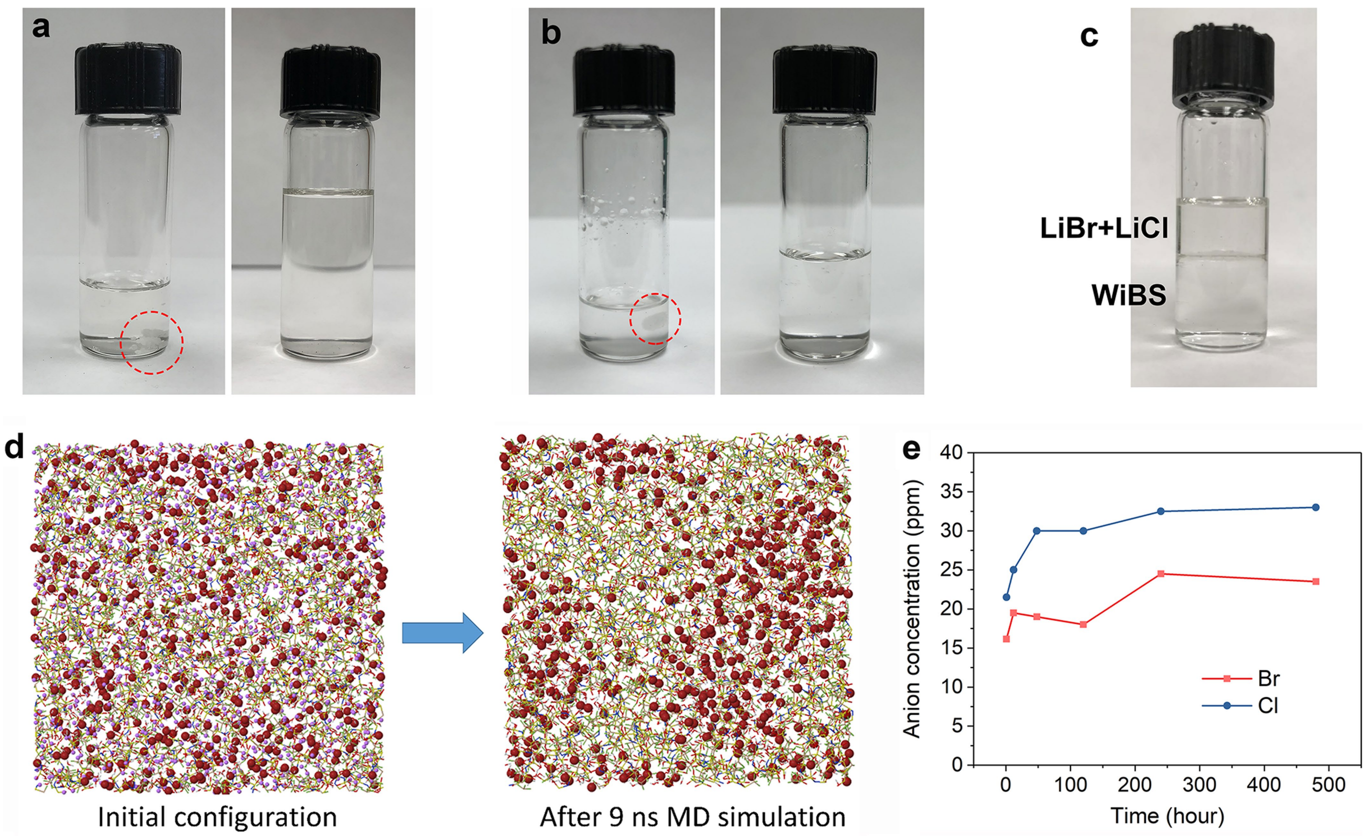

Extended Data Fig. 1 | Immiscibility of LiBr and LiCl in WiBS aqueous electrolyte. **a**, Hydration of anhydrous LiBr/LiCl mixed salts (20 mg, molar ratio 1:1) in 2 g (left) and 5.1 g (right) of WiBS liquid electrolyte. **b**, Hydration of LiBr/LiCl monohydrate mixed salts (20 mg, molar ratio 1:1) in 1.5 g (left) and 3.0 g (right) of WiBS liquid electrolyte. The solid residue is indicated by the dashed circle. **c**, Immiscibility (clear phase separation) of an as-prepared mixture of an aqueous solution (top) of $LiBr{\cdot}3H_2O$ (0.8 g) and $LiCl{\cdot}3H_2O$ (0.4 g) in WiBS liquid electrolyte (bottom; 3 g). **d**, MD simulation cell snapshots, showing the initial configuration (left) and the final configuration (right) after a 9-ns run for a solution of 18 mol kg^{-1} LiBr and 21 mol kg^{-1} LiTFSI in H_2O at 363 K; the Br^- anions are highlighted in red. **e**, Only trace concentrations (<35 p.p.m.) of Br^- and Cl^- are detected in the WiBS liquid electrolyte by anion-exchange liquid chromatography after 500 h of exposure to the LiBr/LiCl solution.

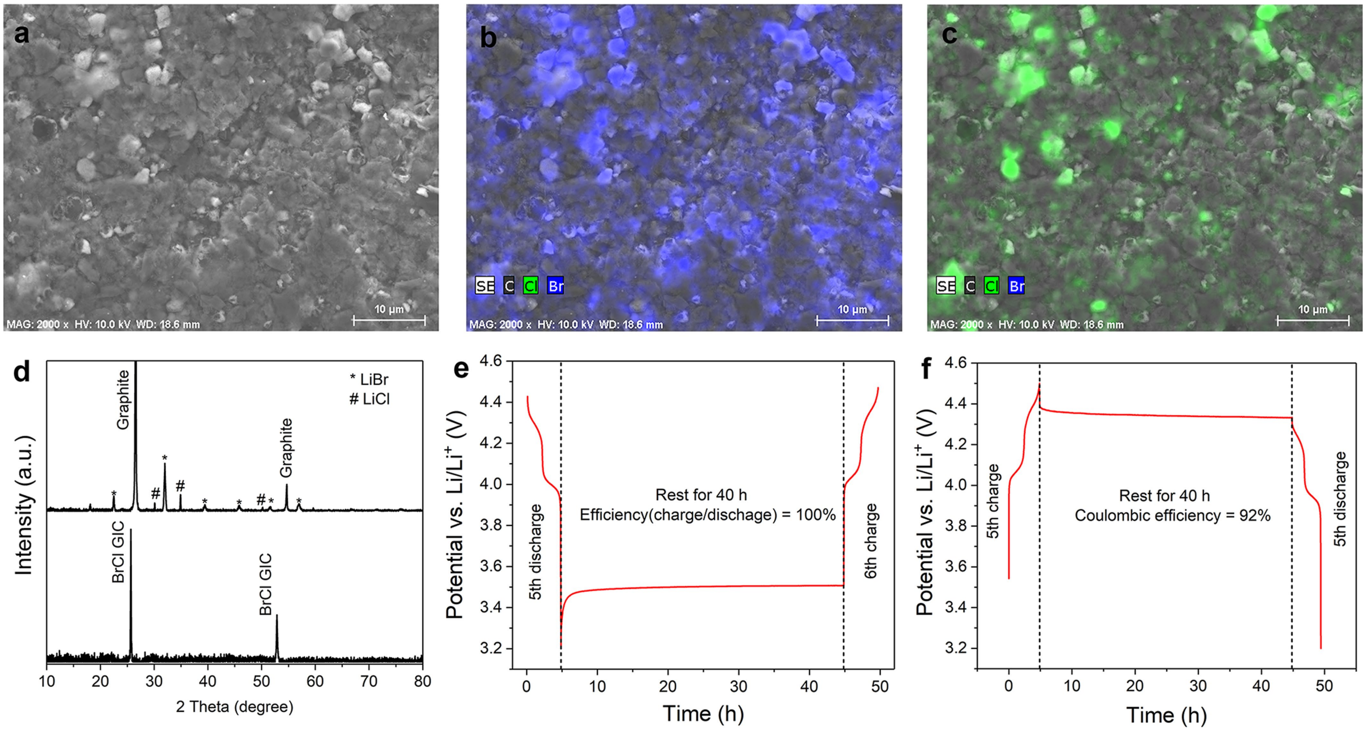

Extended Data Fig. 2 | Solid states of LiBr and LiCl in an LBC-G cathode. a–c, Scanning electron microscope (**a**) and energy-dispersive X-ray spectroscopy mapping (**b**, **c**) images of an LBC-G composite cathode, showing the morphology and elemental distributions of Br (**b**) and Cl (**c**) in the cathode layer after 5 full cycles. The distributions of Br and Cl are overlapping, indicating that the two salts are well mixed as a result of their close association during co-intercalation/de-intercalation. **d**, Ex situ XRD patterns of LBC-G cathodes collected from disassembled cells after the 5th charge and discharge. The disappearance of the LiBr and LiCl peaks and the appearance of the GIC peaks of the LBC-G cathode confirm the BrCl intercalation reaction at the fully charged state, whereas the typical patterns of crystalline LiBr and LiCl at the fully discharged state suggest that solid LiBr and LiCl are reformed after de-intercalation of halogen anions from graphite. The (002) peak of graphite, which has very high intensity, is cut off to show the other peaks. Theta, diffraction angle. **e**, The potential of the LBC-G cathode during discharge, open-circuit relaxation during a 40-h rest, and charging at 0.2 C. The complete recovery of the charge capacity in the next cycle shows that all of the active LiBr and LiCl material was well confined in the LBC-G cathode and there was no capacity loss during the long rest. **f**, The open-circuit voltage decays in the 40-h rest of the LBC-G cathode at the fully charged state of 4.5 V at 0.2 C. Self-discharge was evaluated by comparing with the Coulombic efficiency and the capacity loss after resting.

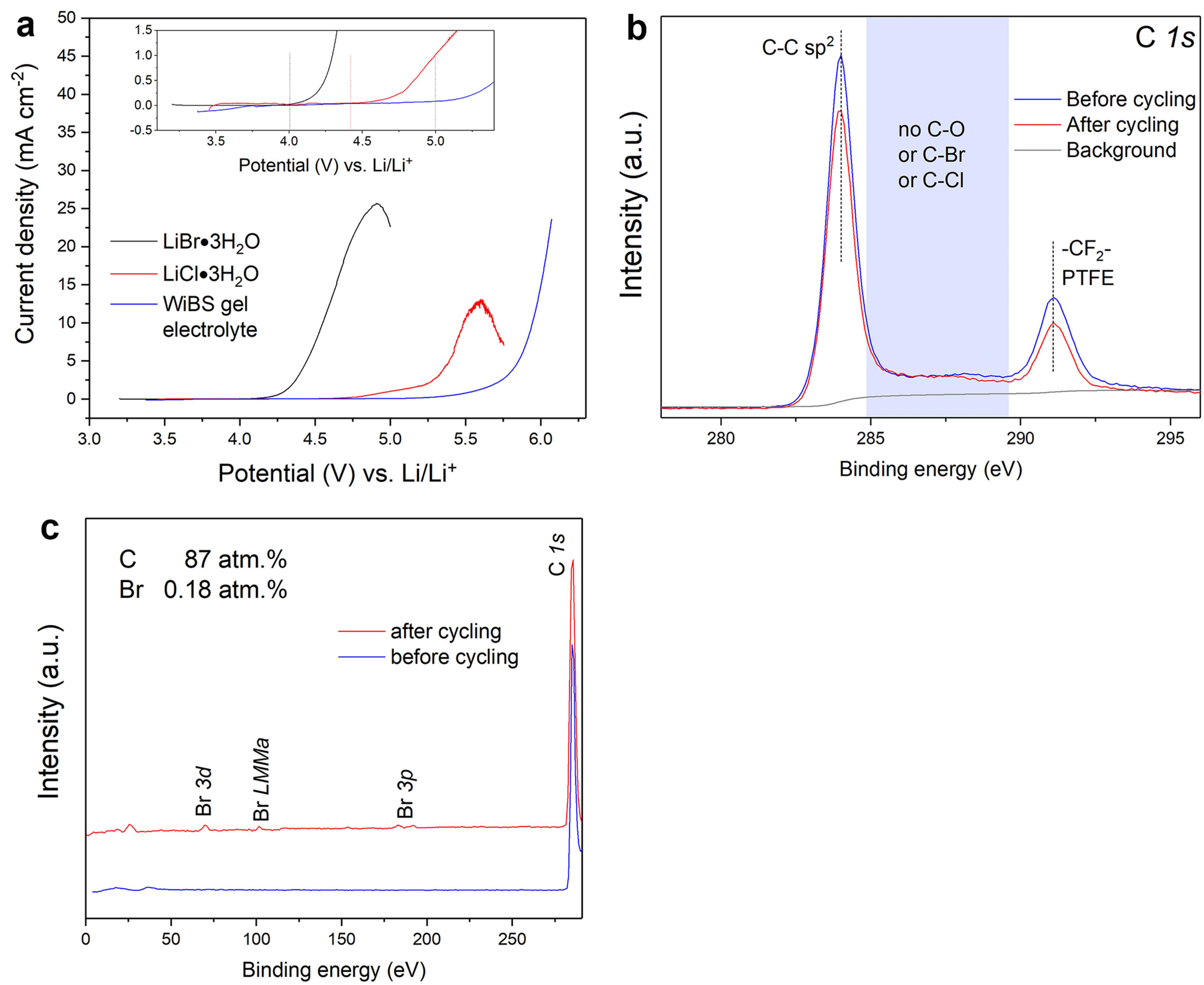

Extended Data Fig. 3 | Absence of corrosion in the current collector and oxidation of graphite and water at the operation potential. **a**, Linear sweep voltammetry of a pure graphite electrode (with only PTFE binder) on a Ti-mesh current collector in $LiBr{\cdot}3H_2O$, $LiCl{\cdot}3H_2O$ and WiBS electrolyte with a Ag/AgCl electrode as reference at 1 mV s^{-1}. The results show absence of side reactions, such as corrosion of the current collector and oxidation of graphite and water, before the onset of the large increase of the current density at about 4.0 V, 4.5 V and 5.0 V versus Li/Li^{+}, in accordance with the oxidation of Br^{-}, Cl^{-} and water, respectively. **b**, **c**, C 1*s* X-ray photoelectron spectra (**b**) and overall spectra (**c**; binding energy of 0–293 eV) of the LBC-G cathode before and after 10 full cycles. LiBr and LiCl were removed to avoid interference. No carbon–oxygen or carbon–halogen bonds were observed. Only traces of Br were detected as intercalation residual.

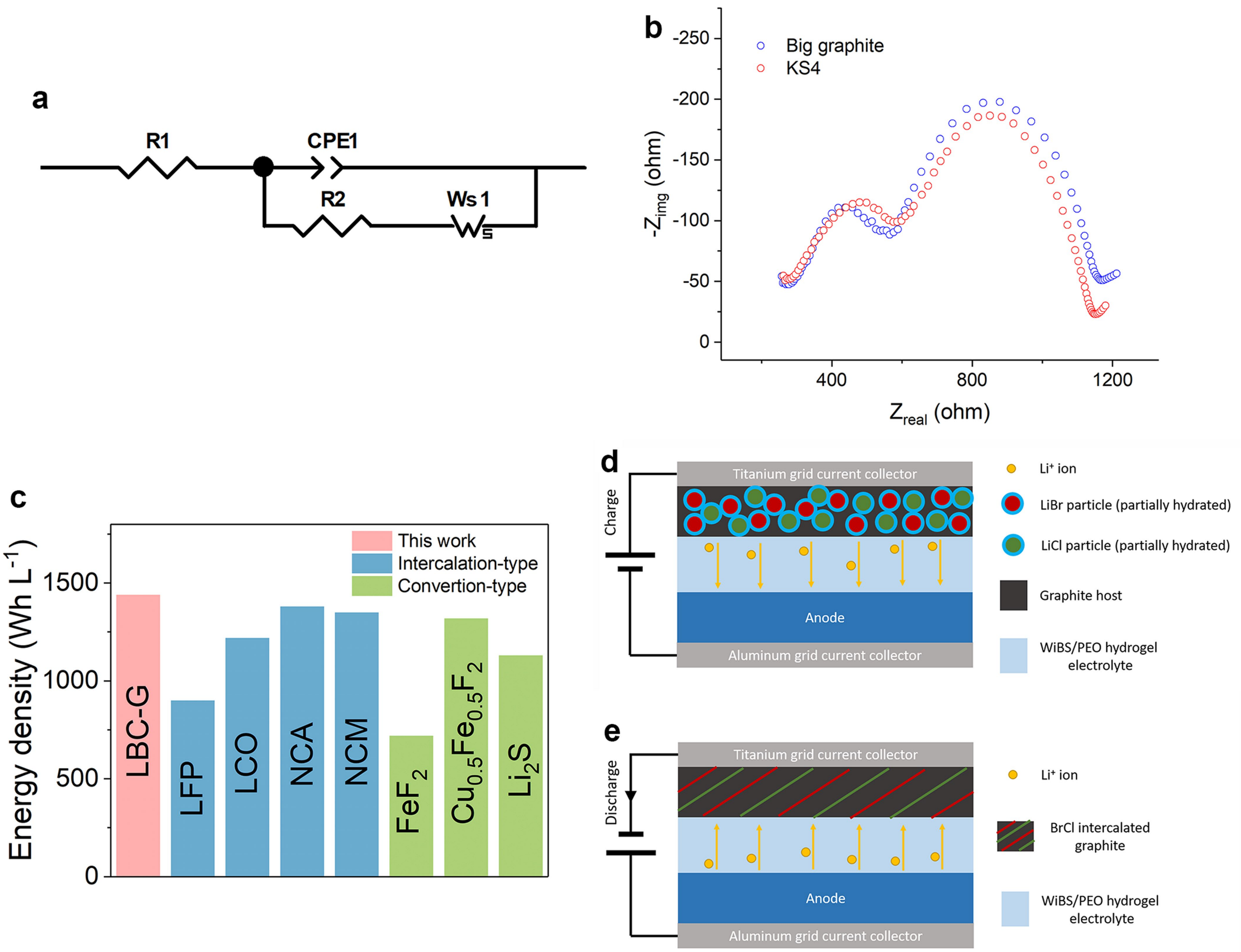

Extended Data Fig. 4 | Nyquist plot fitting, volumetric energy density and full cell configuration. a, Equivalent circuit used for fitting the Nyquist plots in Fig. 1f, consisting of ohmic resistance *R*1 and a constant-phase element (CPE1) parallel to a resistor (*R*2) connected in series with a finite-diffusion Warburg impedance (Ws1). We note that the open Warburg impedance was not included, whereas the data at low frequencies were truncated accordingly during fitting. **b**, Comparison of Nyquist plots of LBC-G cathodes containing graphite hosts with different average flake sizes (KS4, about 4 μm; 'Big graphite', about 800 μm), showing the independence of the diffusion kinetics from the halogen diffusion length inside the graphite interlayer. **c**, Practical volumetric energy density of the LBC-G cathode compared with those of other representative state-of-the-art cathodes when paired with Li metal anodes. For a fair comparison, the potential of a unit stack (the smallest cell unit) comprising a 100-μm-thick cathode, a 9-μm separator and a Li metal anode (average discharge voltages referred to Li/Li^{+}) was calculated using capacity matching. The volume fraction of the active material in each electrode was considered to be 70 vol% for intercalation materials and 60 vol% for conversion-type cathodes. The material properties in the fully expanded (lithiated) state were used to calculate the volumetric capacity and inactive volume within each electrode. The areal capacities of the anodes and cathodes were matched at 1:1 and no extra capacity was considered for formation losses. **d**, **e**, Schematic of the full cell configurations with an LBC-G composite cathode in WiBS aqueous-gel electrolyte during charging (**d**) and discharging (**e**).

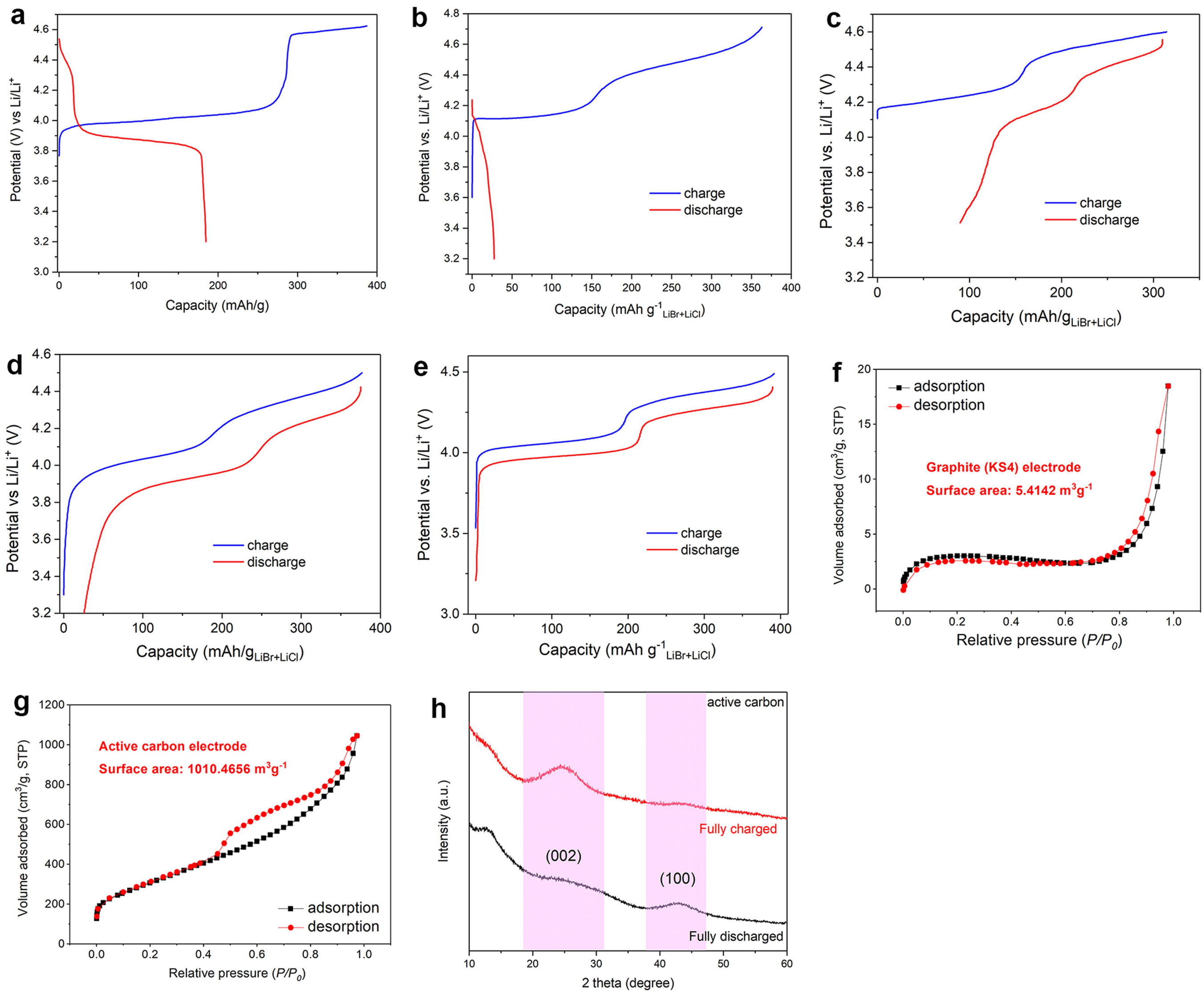

Extended Data Fig. 5 | Reversible halide redox chemistry enabled by intercalation in graphite. Galvanostatic charge and discharge profiles of different composite cathodes at a current density of 80 mA g^{-1} in WiBS gel electrolyte. **a**, LiBr–graphite (mass ratio of about 1:1) cathode in the potential range 3.20–4.62 V. Without the presence of Cl^-, there were no further oxidation reactions of Br^0 until the potential was raised to above 4.55 V versus Li/Li^+, where Br^0 was further irreversibly oxidized into BrO^-. **b**, Composite of $(LiBr)_{0.5}(LiCl)_{0.5}$ and titanium nanopowder (mass ratio 1:20), showing a charge capacity of 85% of the theoretical value for halogen anion redox reactions and negligible discharge capacity. The higher overpotential might be due to the lack of carbon catalysis for the redox reactions. **c**, $(LiBr)_{0.5}(LiCl)_{0.5}$/graphitized carbon black (mass ratio 1:3). **d**, $(LiBr)_{0.5}(LiCl)_{0.5}$/active carbon (mass ratio 1:3). **e**, $(LiBr)_{0.5}(LiCl)_{0.5}$/KS4 (mass ratio 6:4). **f**, **g**, N_2 absorption/desorption isotherm of a graphite (KS4) electrode (**f**) and an active-carbon electrode (**g**) with 5 wt% PTFE binder. The results indicate that, unlike active carbon, the graphite host cannot provide a large surface area and small size pores to store halogens by adsorption. **h**, Ex situ XRD intensity of LiBr/LiCl/active-carbon cathodes at fully charged and discharged states. After adsorbing halogen (Br_2 and BrCl) during charging, a relatively strong peak appears in the (002) peak area, and (100) weakens. This might imply the reformation of randomly oriented small graphitic zones with the help of halogen integration, which indicates a minor contribution of intercalation-like behaviour to halogen storage into nano-graphitized grains.

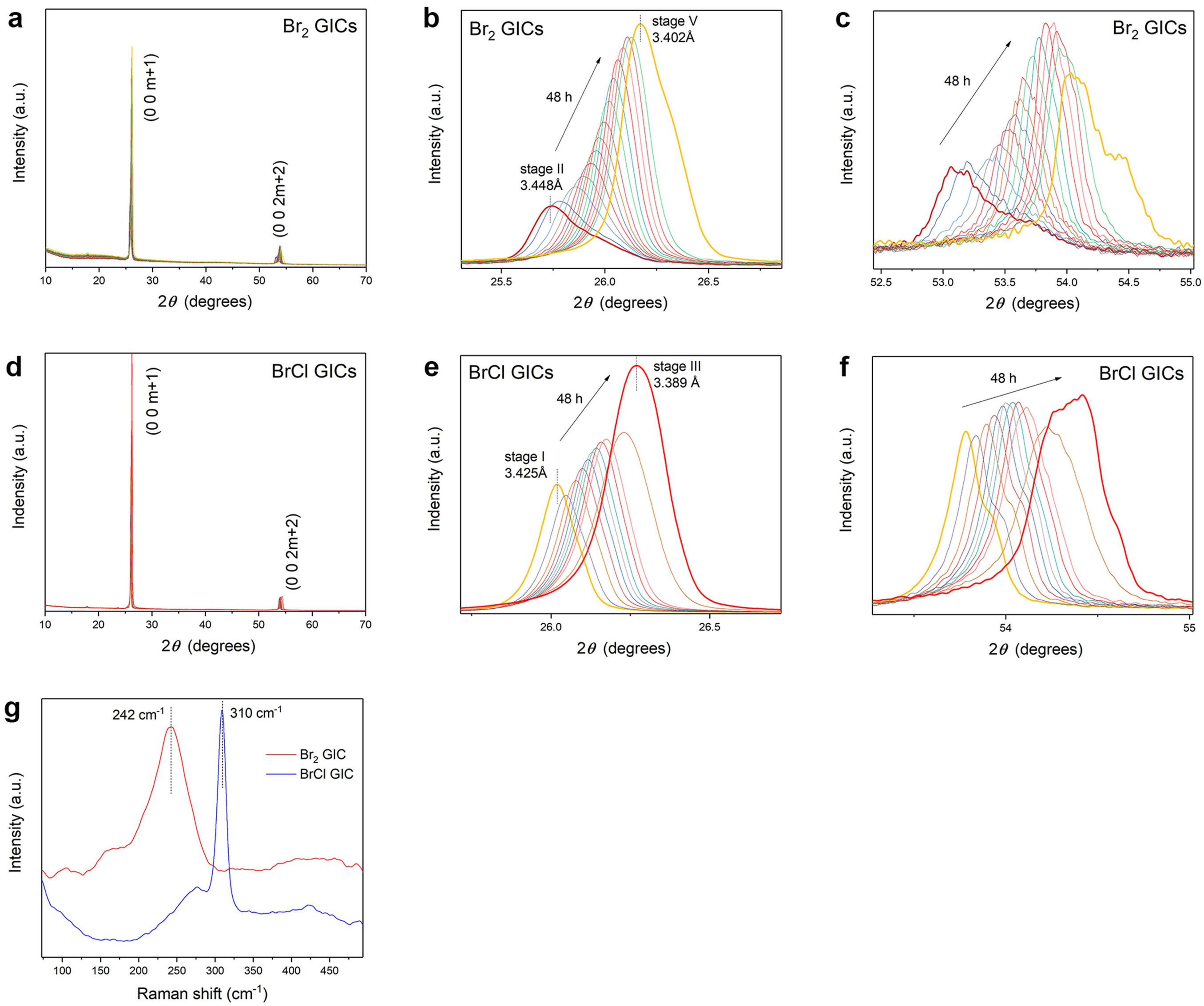

Extended Data Fig. 6 | Reference samples of chemically intercalated halogen GICs. a–f, XRD patterns of chemically intercalated Br_2 (**a–c**) and BrCl (**d–f**) GICs used as reference samples. These GICs were prepared by exposing the graphite flakes in high-concentration Br_2 vapour and BrCl gas for 2 h (more synthesis details in Methods). The spontaneous slow de-intercalations of the XRD peaks that appear at 48 h were observed using the θ–2θ scan mode with Cu Kα radiation (1.5418 Å) in reflection geometry. **g**, Raman spectra (50–500 cm^{-1}) of chemically intercalated Br_2 and BrCl GICs used as reference samples.

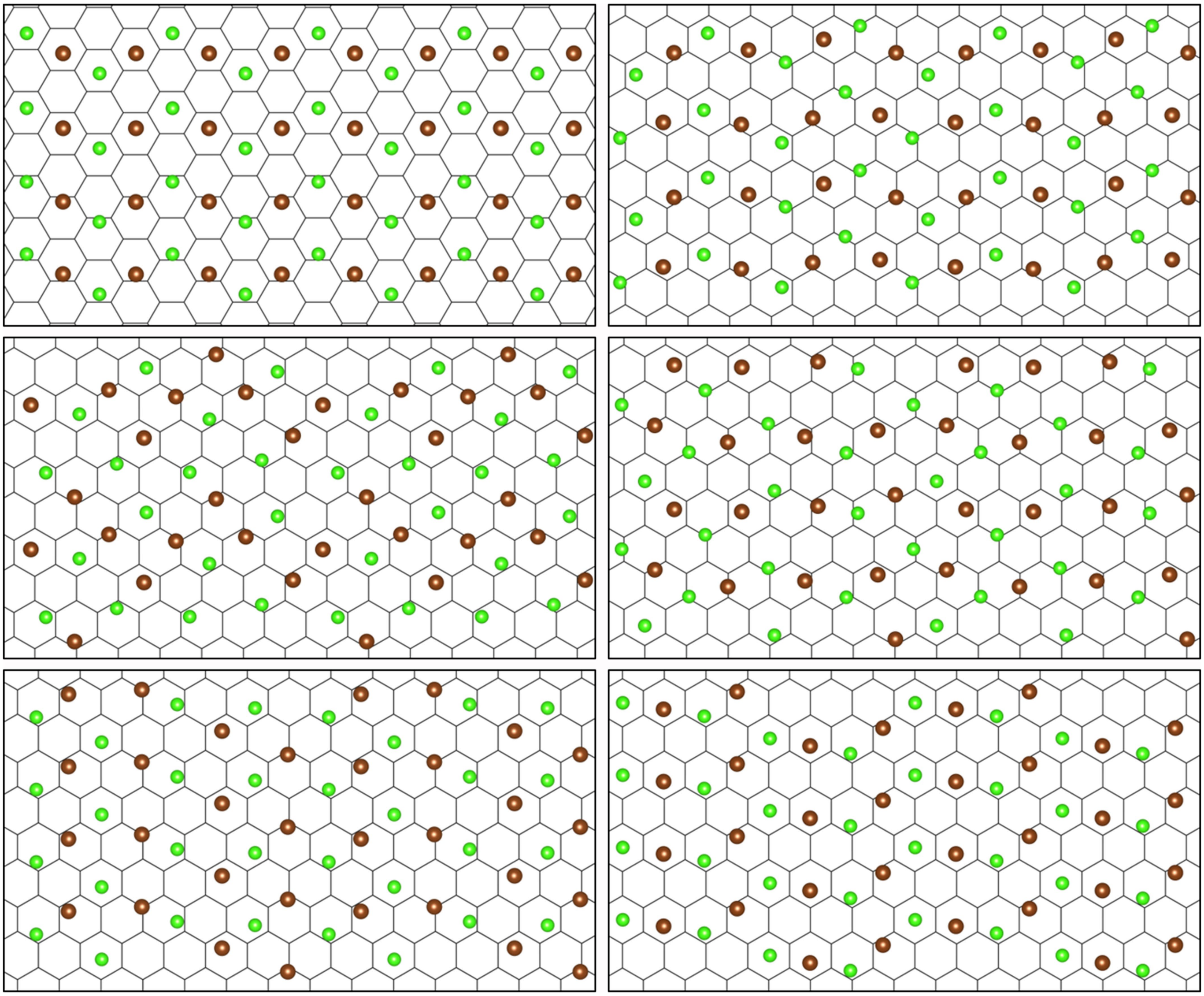

Extended Data Fig. 7 | Representative structures of stage-I [$Br_{0.5}Cl_{0.5}$] $C_{3.5}$ complex obtained from DFT simulations. All structures have intercalation voltages within 0.02 V per ion of a structure with homogenous Br–Cl–Br–Cl bond lengths of 2.45 Å (top left). The bottom right structure is simulated on the basis of the reported Br_2 structure[28]. Quantum chemistry calculations performed on a Cl–Br···Cl–Br cluster surrounded by conductive polarized continuum also yielded a zig-zag configuration for the Cl–Br···Cl–Br complex with a Cl–Br···Cl–Br angle of around 110°, which has lower energy than the linear Cl–Br···Cl–Br configuration by 0.1 eV according to MP2/aug-cc-pvTz and PBE/aug-cc-pvTz calculations. The most stable geometry obtained from these cluster calculations is similar to that found in the stage-I complexes shown above.

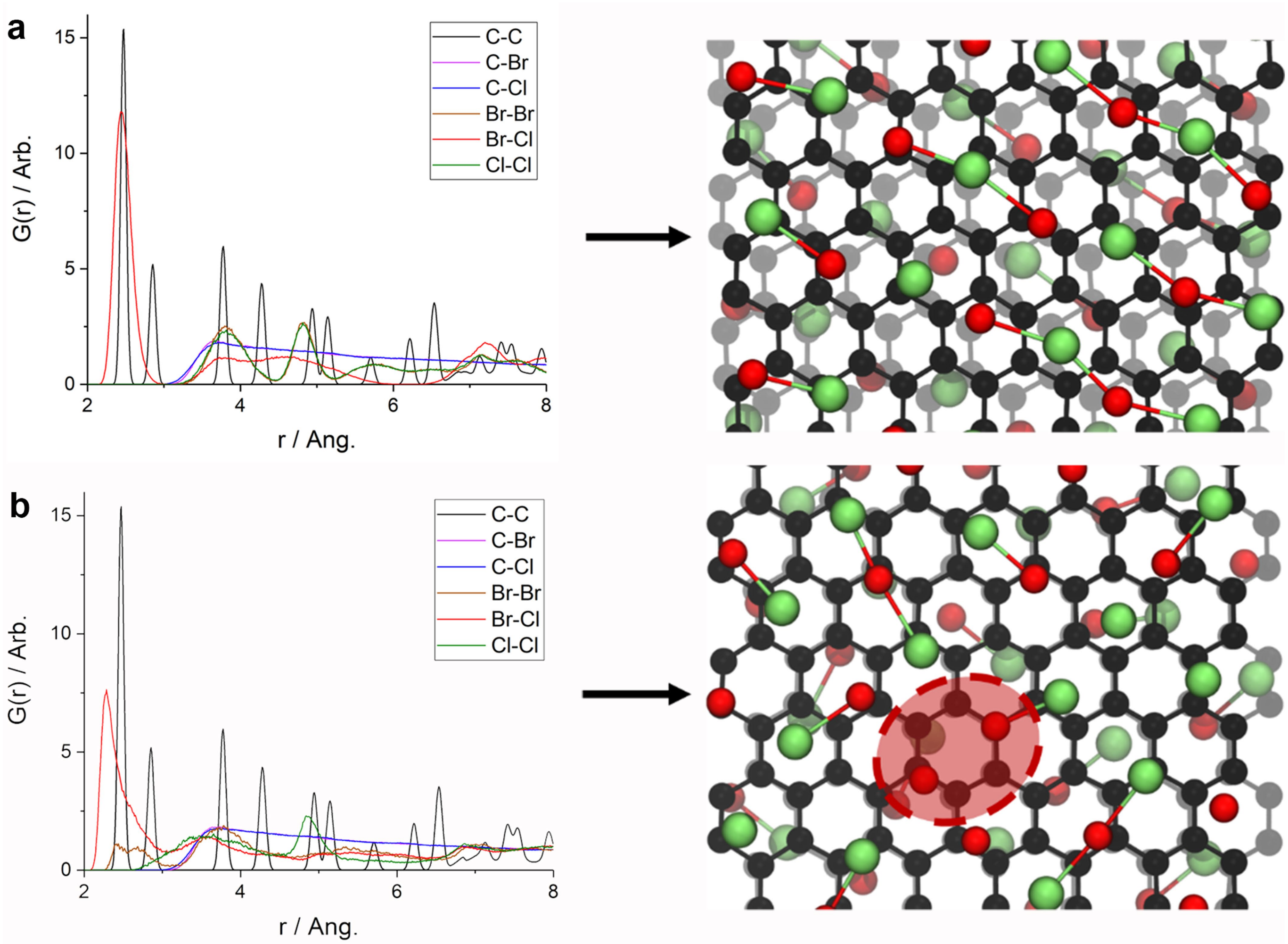

Extended Data Fig. 8 | Stage-I $[Br_{0.5}Cl_{0.5}]C_{3.5}$ complex structures obtained from ab initio MD simulations. Results from 30 ps of NVT ab initio MD simulations using the CP2K package and starting from a structure with homogenous –Br–Cl– bond lengths, as this structure was the most computationally efficient. **a**, Radial distribution function $g(r)$ of stage-I $[Br_{0.5}Cl_{0.5}]C_{3.5}$ from 30 ps of MD simulations at 333 K (left) and final snapshot of the trajectory (right). **b**, DFT results for stage-I $[Br_{0.5}Cl_{0.5}]C_{3.5}$ from 30 ps of simulations at 333 K, following initial annealing at 633 K to accelerate the appearance of disorder (left) and final snapshot of the trajectory (right), with a close Br–Br contact highlighted in red. No close Cl–Cl contacts form at this voltage, as evidenced by the absence of features near the gas-phase Cl–Cl bond length in the radial distribution function. NVT simulations used the Langevin thermostat with an associated time constant of 10 fs and average box dimensions obtained from the equilibration runs performed in the NPT ensemble for 100 ps. A 1 fs timestep was used throughout. No signs of gassing and subsequent graphite exfoliation were observed over 100 ps of additional simulations under constant-pressure conditions, even after brief annealing at 633 K and relaxation back to 333 K.

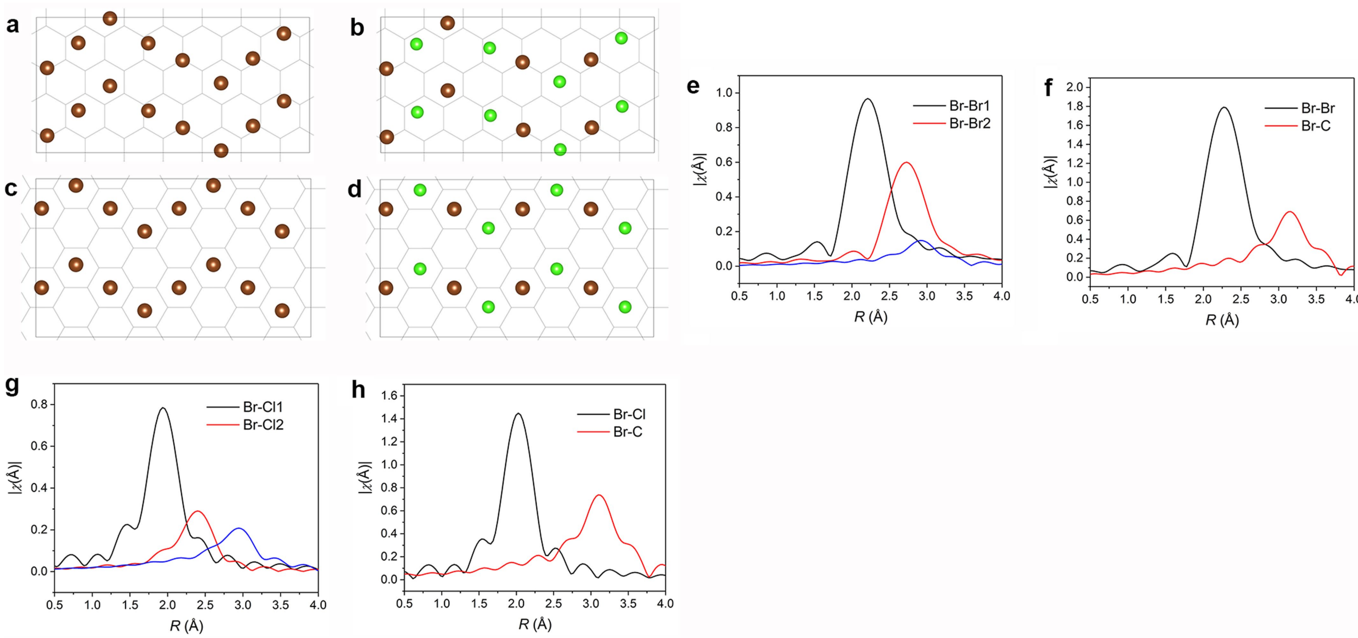

Extended Data Fig. 9 | Representative in-plane configurations of the cathode structure from DFT calculations. a–d, Stage-II C_7[Br] (**a**), stage-I C_7[BrCl] (**b**), stage-II C_8[Br] (**c**) and stage-I C_8[BrCl] (**d**) cathodes obtained from DFT simulations. Only a single set of bond lengths can be obtained with this C_4[X] stoichiometry (X, halogen). **e–h**, Comparison of scattering paths calculated using FEFF6 with different DFT structures to determine the best modes for fitting the experimental XAFS data: stage-II C_7[Br] (**e**) and C_8[Br] (**f**), and stage-I $C_{3.5}[Br_{0.5}Cl_{0.5}]$ (**g**) and $C_4[Br_{0.5}Cl_{0.5}]$) (**h**). The nearest (black), second-nearest (red) and third-nearest (blue) scattering paths around the Br centre are shown. The absence of the second-nearest Br–Br ($R \approx 2.6$ Å) and Br–Cl ($R \approx 2.6$ Å) scattering paths for the C_4[X] stoichiometry suggests that the stoichiometry of $C_{3.5}$[X] would be the dominant one in the real materials.

Extended Data Table 1 | Calculated *d* spacing, stage numbers and plane index of Br_2 and BrCl GICs

Plane index	(002)	(003)	(004)	(005)	(006)	(007)	(008)
Br_2 Stage I	3.5	2.333333	1.75	1.4	1.166667	1	0.875
Br_2 Stage II	5.175	3.45	2.5875	2.07	1.725	1.478571	1.29375
Br_2 Stage III	6.85	4.566667	3.425	2.74	2.283333	1.957143	1.7125
Br_2 Stage IV	8.525	5.683333	4.2625	3.41	2.841667	2.435714	2.13125
Br_2 Stage V	10.2	6.8	5.1	4.08	3.4	2.914286	2.55
Br_2 Stage VI	11.875	7.916667	5.9375	4.75	3.958333	3.392857	2.96875
Br_2 Stage VII	13.55	9.033333	6.775	5.42	4.516667	3.871429	3.3875
BrCl Stage I	3.425	2.283333	1.7125	1.37	1.141667	0.978571	0.85625
BrCl Stage II	5.1	3.4	2.55	2.04	1.7	1.457143	1.275
BrCl Stage III	6.775	4.516667	3.3875	2.71	2.258333	1.935714	1.69375
BrCl Stage IV	8.45	5.633333	4.225	3.38	2.816667	2.414286	2.1125
BrCl Stage V	10.125	6.75	5.0625	4.05	3.375	2.892857	2.53125
BrCl Stage VI	11.8	7.866667	5.9	4.72	3.933333	3.371429	2.95
BrCl Stage VII	13.475	8.983333	6.7375	5.39	4.491667	3.85	3.36875

Values corresponding to the dominant XRD peaks are marked in red. The results were calculated using equation (6).